Geophysical Journal International

Geophys. J. Int. (2025) **00,** 1–14
GJI General Geophysical Methods

https://doi.org/10.1093/gji/ggaf110

Theory and simulation for low-frequency interfacial polarization of plant root cell

Satoshi Izumoto and Frédéric Nguyen

Faculty of Applied Sciences, Urban and Environmental Engineering Department, University of Liège, B-4000 Liège, Belgium. E-mail: Satoshi.Izumoto@uliege.be

Accepted 2025 March 21. Received 2025 March 18; in original form 2024 September 28

SUMMARY

The intricate architecture of plant root systems is crucial for nutrient and water uptake, significantly influencing plant growth and productivity. Induced polarization is a promising non-destructive technique for analysing plant roots in their natural conditions. This study introduces a novel theoretical and numerical model to explain the significant low-frequency polarization of plant root cells observed in previous experiments. Our approach addresses the limitations of existing models by incorporating geometric constraints and internal mechanisms of cell polarization, particularly focusing on interfacial polarization across the cell membrane. Through comprehensive simulations, we investigate various geometries and boundary conditions, demonstrating that densely packed root cells exhibit significant polarization signals within a measurable frequency range due to coupling effects. Our findings align with experimental observations, indicating that the peak frequency is highly sensitive to cell arrangement and membrane properties, while the maximum phase shift remains consistent. This model provides a robust framework for interpreting polarization signals in root systems, offering potential applications for *in-situ* characterization of plant roots and enhancing the understanding of root dynamics under different environmental conditions.

Key words: Induced polarization; Numerical modelling; Hydrogeophysics..

1 INTRODUCTION

The intricate architecture of plant root systems is crucial for nutrient and water uptake, directly influencing plant growth, health and productivity (Taiz & Zeiger 2002). This subterranean component of the plant, often dubbed the 'hidden half', plays a pivotal role in the soil-plant-atmosphere continuum, mediating various biogeochemical cycles and soil interactions. In laboratories, roots can be studied using techniques such as magnetic resonance imaging, X-ray computed tomography and positron emission tomography (Atkinson *et al.* 2019; Tracy *et al.* 2020; Griffiths *et al.* 2022; Hou *et al.* 2022). However, examining these root systems in their natural field conditions without causing harm or disturbing the environment has long been a challenge for researchers and agronomists. This has led to the development of innovative, non-destructive methods that allow for insights into root structure and function (Ehosioke *et al.* 2020). One such method involves measuring the spectral impedance by attaching an electrode to the plant and inserting another into the soil, utilizing the dielectric properties of the roots (Dalton 1995; Ozier-Lafontaine & Bajazet 2005; Cao *et al.* 2011; Dietrich *et al.* 2012; Cseresnyés *et al.* 2013; Peruzzo *et al.* 2021; Cseresnyés *et al.* 2022). Although this technique has shown promise, it is limited to analysing one plant at a time. In addition, some studies have highlighted the importance of current leakage from the proximal part. This means that the electric current might enter the soil without passing through the root (e.g. Dietrich *et al.* 2012; Peruzzo *et al.* 2021).

Geophysical measurements, including electrical resistivity tomography (ERT), offer ways to detect subsurface root systems over large areas (Cimpoiaşu *et al.* 2020; Ehosioke *et al.* 2020; Liu *et al.* 2021). However, ERT often faces challenges due to the low contrast between the roots and surrounding soil, influenced by the low volume of roots and variations in soil resistivity (Ehosioke *et al.* 2020). Since roots and soil grains are not naturally conductive, distinguishing between them using ERT is challenging. Recent advancements in techniques like induced polarization (IP), impedance tomography and impedance spectroscopy have demonstrated potential for detailed *in-situ* analysis of root systems (Kessouri *et al.* 2019; Cimpoiaşu *et al.* 2020; Ehosioke *et al.* 2020; Tsukanov & Schwartz 2020; Liu *et al.* 2021). These methods, by embedding electrodes in the soil, can provide essential spatial information both at the surface and in depth. Experimental studies have shown that root cells can produce significant polarization signals, indicating a high sensitivity of these methods to the presence of roots (Mary *et al.* 2017; Weigand & Kemna 2017, 2019; Ehosioke *et al.* 2023). Interestingly, when roots are measured directly, the magnitude of their response is comparable to that of metal grains (Ozier-Lafontaine & Bajazet 2005; Cseresnyés *et al.* 2013; Peruzzo *et al.* 2021; Ehosioke

et al. 2023). Since metals are traditionally the primary focus of IP measurements, the fact that roots elicit a similarly strong response is promising. The surrounding soil exhibits different IP responses depending on factors such as water content and organic matter (e.g. Breede *et al.* 2011; Schwartz *et al.* 2014). Since roots exhibit a strong IP response, we expect this to dominate variations if measured accurately, similar to the case of disseminated iron, where even a small amount in geological material can produce a large response (e.g. Abdel Aal *et al.* 2014; Gurin *et al.* 2015). A previous study (Weigand *et al.* 2022) attempted to detect herbaceous plant roots in field measurements, and in our view, the results suggest that further improvements (e.g. Wang *et al.* 2021; Weigand *et al.* 2022; Wang *et al.* 2024) are needed to refine the measurement system for shallow soil with greater spatial resolution. Although this remains a technical challenge, it lies beyond the scope of our study.

Many existing models simplify root cells as elements in an electrical circuit or as spherical cells diluted in water (Mancuso 2012; Bera *et al.* 2016; Cseresnyés *et al.* 2017; Gu *et al.* 2024). These models assign empirically determined properties such as complex permittivity, conductivity or impedance to the root cells. Consequently, they do not adequately explain the internal mechanisms by which cells polarize. The polarization of plant root cell based on traditional models (Tsukanov & Schwartz 2021), centred around the polarization inside electrical double layer concept, have fallen short in explaining the magnitude of polarization signals in experiments (Ozier-Lafontaine & Bajazet 2005; Cseresnyés *et al.* 2013; Peruzzo *et al.* 2021; Ehosioke *et al.* 2023), by several orders of magnitude. This discrepancy points to an incomplete understanding of the complex mechanisms governing root cell polarization and highlights the necessity for a revised theoretical and numerical approach that can better reproduce the experimental results.

In this context, our research introduces a new theoretical and numerical model specifically designed to explain the experimental results concerning root cell polarization by focusing on interfacial polarization of the cell. The interfacial polarization of the cell is a well-established concept, primarily used to calculate the impedance of microbial and blood cells (e.g. Flores-Cosío *et al.* 2020; Turcan & Olariu 2020). It has also been considered a potential source of polarization in plant roots (Bera *et al.* 2016; Bera 2018; Peruzzo *et al.* 2018; Jócsák *et al.* 2019). Our aim here is therefore to obtain a more fundamental understanding of the polarization processes of a single root segment that can reasonably explain both the qualitative and quantitative aspects of previous experimental results. Following the previous study about the effect of geometry and boundary conditions on the polarization of metal grains (Izumoto 2023), we simulated polarization in various geometries such as densely packed cells. In Izumoto (2023), metal grains were modelled with infinitely high conductivity based on the theory of Feng *et al.* (2020). In contrast, cells have limited conductivity within their structure, requiring a different modelling approach. By providing a solid theoretical base and simulation results for the interpretation of polarization signals in root systems, our model paves the way for further investigations into root dynamics with spectroscopic electrical measurements.

2 THEORY

2.1 Deriving analytical solution for a single cell surrounded by water

We considered a cell embedded in water as depicted in Fig. 1. The cell membrane is modelled through its thickness and permittivity.

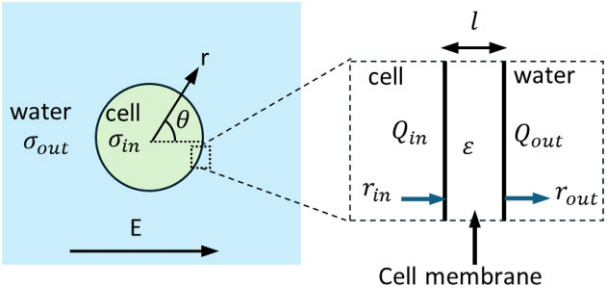

Figure 1. The concept of the model. The cell (green) is in the water (blue). σ_{out} and σ_{in} represent the conductivity outside and inside of cell. E is the electric field direction. r is pointing outward from the centre of the cell. θ is the angle between the direction of electric field E and r. Closed up view of the interface of cell shows the membrane with a thickness of l and permittivity of ε. Q_{in} and Q_{out} are the ions accumulated on the cell membrane inside and outside of the cell. r_{in} is defined inside of the cell, pointing toward membrane. r_{out} is defined outside of the cell, pointing outward from the membrane.

This allows charges to accumulate on both sides of this membrane due to the electric current directed toward it. The membrane itself could be attributed an electrical conductivity (Kotnik & Miklavcic 2000) but we will account here for potential charge transport across the membrane through ion channels. Our focus is on the interfacial polarization across the cell membrane, rather than the polarization on just one side. When positive charge gathers on one side of the membrane, it induces the accumulation of negative charge on the opposite side due to the electric field created by the positive charge. This phenomenon can be linked to the capacitance in an electrical circuit, where capacitance involves a pair of flat metal plates separated by a dielectric material. In our model, the cell membrane functions similarly, with the lipid bilayer acting as the dielectric and being surrounded by conductive solutions. This setup provided the necessary boundary conditions on both sides of the cell membrane.

We built a theoretical model based on the above concept. The electric field satisfies Laplace's equation to ensure the zero divergence of electric current in the absence of source:

$$\nabla^2 \phi = 0 \tag{1}$$

The charge accumulation on the cell membrane is given by:

$$F\frac{\partial Q_{\text{in}}}{\partial t} = -\sigma_{\text{in}}\frac{\partial \phi_{\text{in}}}{\partial r_{\text{in}}}, \tag{2}$$

$$F\frac{\partial Q_{\text{out}}}{\partial t} = \sigma_{\text{out}}\frac{\partial \phi_{\text{out}}}{\partial r_{\text{out}}}, \tag{3}$$

where F is Faraday constant (C mol^{-1}), σ, ϕ are electric conductivity (S m^{-1}), and potential (V) with its subscript indicating either inside or outside of the cell. Q (mol m^{-2}) is the virtual ion concentration accumulated on the surface that is responsible for the excess charge. It means that Q can be negative if the net charge is negative. The partial derivative of r_{in} is defined inside of the cell, taken toward the membrane surface, and that of r_{out} is defined outside of the cell, taken outward from the membrane surface (Fig. 1). Using these coordinates, if the bulk virtual ion concentration outside of the cell is written as $Q_{\text{bulk,out}}$ (mol m^{-3}), it follows $Q_{\text{out}} = \int Q_{\text{bulk,out}} dr_{\text{out}}$. Similar equation holds for inside too. Note that the right-hand side of eqs (2) and (3) can be interpreted as electric current flowing toward the membrane surface. From the concept (Fig. 1), the potential difference across the membrane was given by

$$\phi_{\text{in}} = \phi_{\text{out}} - \frac{Fl}{\varepsilon} Q_{\text{out}}, \tag{4}$$

$$\phi_{\text{out}} = \phi_{\text{in}} - \frac{Fl}{\varepsilon} Q_{\text{in}}, \tag{5}$$

where l is the thickness of the membrane and ε is the permittivity of the membrane. Replacing the Q in eqs (2), (3) by eqs (4), (5):

$$\frac{\partial \phi_{\text{out}}}{\partial t} = \frac{\partial \phi_{\text{in}}}{\partial t} + \frac{l\sigma_{\text{in}}}{\varepsilon} \frac{\partial \phi_{\text{in}}}{\partial r_{\text{in}}}, \tag{6}$$

$$\frac{\partial \phi_{\text{in}}}{\partial t} = \frac{\partial \phi_{\text{out}}}{\partial t} - \frac{l\sigma_{\text{out}}}{\varepsilon} \frac{\partial \phi_{\text{out}}}{\partial r_{\text{out}}}. \tag{7}$$

These equations were used to derive equations for numerical simulations later.

Biological cell has ion channels that facilitate ion exchange between inside and outside of the cell (Taiz & Zeiger 2002). We modelled such channels as holes to pass the accumulated charges through the cell membrane. Such charge transport is driven by the potential difference between inside and outside of the cell. Thus, eqs (2) and (3) were modified as:

$$F \frac{\partial Q_{\text{in}}}{\partial t} = -\sigma_{\text{in}} \frac{\partial \phi_{\text{in}}}{\partial r_{\text{in}}} + \alpha \left(\phi_{\text{out}} - \phi_{\text{in}}\right), \tag{8}$$

$$F \frac{\partial Q_{\text{out}}}{\partial t} = \sigma_{\text{out}} \frac{\partial \phi_{\text{out}}}{\partial r_{\text{out}}} - \alpha \left(\phi_{\text{out}} - \phi_{\text{in}}\right) \tag{9}$$

with α in eqs (8) and (9) representing the ability of the channel to transport the charge across the membrane. Note that α could be frequency dependent but we did not consider yet this assumption in this work. In a later section, we will determine whether α is negligible by using the highest conductivity value across the membrane reported in the literature. From eqs (4), (5), (8) and (9), we replace the charge terms to obtain:

$$\frac{\partial \phi_{\text{out}}}{\partial t} = \frac{\partial \phi_{\text{in}}}{\partial t} + \frac{l\sigma_{\text{in}}}{\varepsilon} \left(\frac{\partial \phi_{\text{in}}}{\partial r_{\text{in}}} - \frac{\alpha}{\sigma_{\text{in}}} \left(\phi_{\text{out}} - \phi_{\text{in}}\right) \right), \tag{10}$$

$$\frac{\partial \phi_{\text{in}}}{\partial t} = \frac{\partial \phi_{\text{out}}}{\partial t} - \frac{l\sigma_{\text{out}}}{\varepsilon} \left(\frac{\partial \phi_{\text{out}}}{\partial r_{\text{out}}} - \frac{\alpha}{\sigma_{\text{out}}} \left(\phi_{\text{out}} - \phi_{\text{in}}\right) \right). \tag{11}$$

Let us consider the spherical cell in uniform sinusoidal electric potential. The centre of the cell was set as zero potential. In spherical coordinate, the applied potential is written as $E_0\, r \cos\theta\, e^{i\omega t}$, where ω is the angular frequency (rad s^{-1}). The analytical solution can be written in the form of spherical harmonics (MacRobert 1967):

$$\phi_{\text{in}} = \sum_{l=1}^{\infty} a_l r^l P_l e^{i\omega t}, \tag{12}$$

$$\phi_{\text{out}} = -\left(E_0 r \cos\theta + \sum_{l=1}^{\infty} B_l r^{-(l+1)} P_l \right) e^{i\omega t}, \tag{13}$$

where P_l represents Legendre polynomials, a_l and B_l are its coefficients. The boundary conditions on the membrane surface, eqs (11) and (10) determined the coefficients of the Legendre polynomials as:

$$B_l = \begin{cases} \frac{R^3((1-\sigma_r)\beta + 2A\sigma_r)}{2\beta + 4A\sigma_r + \sigma_r \beta} E_0 & \text{if } l = 1 \\ 0 & \text{otherwise} \end{cases}, \tag{14}$$

where

$$A = \frac{l\sigma_{\text{out}}}{2\varepsilon}, \tag{15}$$

$$\sigma_r = \frac{\sigma_{\text{in}}}{\sigma_{\text{out}}}, \tag{16}$$

$$\beta = i\omega R + \frac{2A\alpha R}{\sigma_{\text{out}}} \tag{17}$$

and R is the radius of the spherical cell. The coefficients inside the cell is:

$$a_l = \begin{cases} -\left(\frac{1}{R^3} + \frac{4A}{\beta R^3}\right) B_l + \left(\frac{2A}{\beta} - 1\right) E_0 & \text{if } l = 1 \\ 0 & \text{otherwise} \end{cases}. \tag{18}$$

Thus, we obtained the solutions:

$$\phi_{\text{in}} = a_1 r \cos\theta e^{i\omega t}, \tag{19}$$

$$\phi_{\text{out}} = -\left(E_0 r + B_1 r^{-2}\right) \cos\theta e^{i\omega t} \tag{20}$$

with a_1 and B_1 given by the above equations. The above equations include many parameters. We reduced the number of parameters by introducing non-dimensional form as summarized in Table 1. In non-dimensional form, the potential outside the cell is:

$$\phi^*_{\text{out}} = -\left(r' + B^*_1 r'^{-2}\right) \cos\theta e^{i\omega t} \tag{21}$$

with

$$B^*_1 = \frac{(1-\sigma_r)(i\omega^* + 2\alpha^*) + 2\sigma_r}{2(i\omega^* + 2\alpha^*) + 4\sigma_r + \sigma_r(i\omega^* + 2\alpha^*)}, \tag{22}$$

where the non-dimensional variables were defined as $\phi^*_{\text{out}} = \phi_{\text{out}}/RE_0$, $r' = r/R$, $\omega^* = \omega R/A$, $\alpha^* = \alpha R/\sigma_{\text{out}}$. This also suggests the following useful relationship between frequency and parameters:

$$\omega \propto \frac{A}{R} = \frac{l\sigma_{\text{out}}}{2R\varepsilon}. \tag{23}$$

For the potential inside the cell,

$$\phi^*_{\text{in}} = a^*_1 r' \cos\theta e^{i\omega t} \tag{24}$$

with

$$a^*_1 = -\left(1 + \frac{4}{i\omega^* + 2\alpha^*}\right) B^*_1 + \left(\frac{2}{i\omega^* + 2\alpha^*} - 1\right), \tag{25}$$

where the non-dimensional potential was defined as $\phi^*_{\text{in}} = \phi_{\text{in}}/RE_0$.

Based on these results, we calculated at which frequency ϕ'' takes peak value on the surface of the cell. At this frequency, termed as peak frequency, on the surface ($r = R$), $\frac{\partial(\text{Im}(\phi))}{\partial\omega} = 0$. We obtained the peak frequency as:

$$\omega_{c,\phi''} = \frac{2A\left(\frac{2\alpha R}{\sigma_{\text{out}}} + 2\sigma_{\text{r}} + \frac{\alpha R \sigma_{\text{r}}}{\sigma_{\text{out}}}\right)}{R(2 + \sigma_{\text{r}})}. \tag{26}$$

In non-dimensional form, it becomes

$$\omega^*_{c,\phi''} = 2(\alpha^* + 2) - \frac{8}{\sigma_{\text{r}} + 2} \tag{27}$$

with $\omega^*_{c,\phi''} = \omega_{c,\phi''} R/A$. For $\alpha^* = 0$ (no ion channel, see eqs 8 and 9), the above equation can be written as:

$$\omega^*_{c,\phi'',\alpha=0} = \frac{4\sigma_{\text{r}}}{2 + \sigma_{\text{r}}}. \tag{28}$$

At this frequency, ϕ'' can be calculated as:

$$\phi''_{\text{peak}} = -\frac{3R\sigma_{\text{r}}^2}{2(2 + \sigma_{\text{r}})\left(\frac{2\alpha R}{\sigma_{\text{out}}} + 2\sigma_{\text{r}} + \frac{\alpha R \sigma_{\text{r}}}{\sigma_{\text{out}}}\right)} E_0. \tag{29}$$

In non-dimensional form, the above equation becomes

$$\phi''^*_{\text{peak}} = -\frac{3\sigma_{\text{r}}^2}{2(2 + \sigma_{\text{r}})(2\alpha^* + 2\sigma_{\text{r}} + \alpha^*\sigma_{\text{r}})} \tag{30}$$

with $\phi''^*_{\text{peak}} = \phi''_{\text{peak}}/RE_0$. For $\alpha^* = 0$:

$$\phi''^*_{\text{peak},\alpha=0} = -\frac{3\sigma_{\text{r}}}{4(2 + \sigma_{\text{r}})} \tag{31}$$

Table 1. The list of parameters used in the analytical solutions, and the conversion from dimensional variables to dimensionless variables.

	Potential	Frequency	Coordinate	Conductivity	Membrane conductivity	Permittivity Electric field Radius Membrane thickness	Phase shift
Dimensional	$\phi_{\text{in}}, \phi_{\text{out}}, \phi', \phi''$	ω	r	$\sigma_{\text{in}}, \sigma_{\text{out}}$	α	ε, E_0, R, l	
Dimensionless	$\phi^*_{\text{in}}, \phi^*_{\text{out}}, \phi'^*, \phi''^*$	ω^*	r'	σ_r	α^*	–	Φ
Conversion from dimensional to dimensionless	Divide by RE_0	$\omega^* = 2\varepsilon\omega R/l\sigma_{\text{out}}$	Divide by R	$\sigma_r = \sigma_{\text{in}}/\sigma_{\text{out}}$	$\alpha^* = \alpha R/\sigma_{\text{out}}$	–	–

Notably, the above equation is independent of A (defined in eq. 15), suggesting the independence of peak ϕ'' to the properties of membrane such as thickness and permittivity. The phase shift, defined by $\Phi = \arctan\left(\frac{\text{Im}(\phi)}{\text{Re}(\phi)}\right)$, at the surface was calculated in a similar manner. At the peak phase shift, $\frac{\text{Im}(\phi)}{\text{Re}(\phi)}$ takes the peak value. Thus, at this frequency, $\frac{\partial(\text{Im}(\phi)/\text{Re}(\phi))}{\partial\omega} = 0$. Solving this equation led to:

$$\omega_{c,\Phi} = \frac{2A}{R}\left(\frac{\left(\frac{2\alpha R}{\sigma_{\text{out}}} + 2\sigma_{\text{r}} + \frac{\alpha R\sigma_{\text{r}}}{\sigma_{\text{out}}}\right)\left(\frac{\alpha R}{\sigma_{\text{out}}} + \sigma_{\text{r}}\right)}{2+\sigma_{\text{r}}}\right)^{1/2} \tag{32}$$

In non-dimensional form,

$$\omega^*_{c,\Phi} = 2\left(\frac{(2\alpha^* + 2\sigma_{\text{r}} + \alpha^*\sigma_{\text{r}})(\alpha^* + \sigma_{\text{r}})}{2+\sigma_{\text{r}}}\right)^{1/2} \tag{33}$$

with $\omega^*_{c,\Phi} = \omega_{c,\Phi}R/A$. For $\alpha^* = 0$,

$$\omega^*_{c,\Phi,\alpha=0} = 2\sigma_{\text{r}}\left(\frac{2}{2+\sigma_{\text{r}}}\right)^{1/2} \tag{34}$$

At this peak frequency, the phase shift can be calculated as:

$$\begin{aligned}\Phi_{peak} &= \arctan\left(-\frac{\sigma_{\text{r}}^2}{2\left(\left(\frac{2\alpha R}{\sigma_{\text{out}}} + 2\sigma_{\text{r}} + \frac{\alpha R\sigma_{\text{r}}}{\sigma_{\text{out}}}\right)\left(\frac{\alpha R}{\sigma_{\text{out}}} + \sigma_{\text{r}}\right)(2+\sigma_{\text{r}})\right)^{\frac{1}{2}}}\right) \\ &= \arctan\left(-\frac{\sigma_{\text{r}}^2}{2\left((2\alpha^* + 2\sigma_{\text{r}} + \alpha^*\sigma_{\text{r}})(\alpha^* + \sigma_{\text{r}})(2+\sigma_{\text{r}})\right)^{\frac{1}{2}}}\right)\end{aligned} \tag{35}$$

For $\alpha^* = 0$, the equation becomes:

$$\Phi_{peak} = \arctan\left(-\frac{\sigma_{\text{r}}}{4}\left(\frac{2}{2+\sigma_{\text{r}}}\right)^{\frac{1}{2}}\right) \tag{36}$$

The above equation suggests that Φ_{peak} is independent of membrane properties, represented by A, as well as the size of the cell R.

2.2 Analysing and comparing the analytical solution of a single cell to experimental data

2.2.1 Potential distribution

From the analytical solutions given in eqs (21), (22), (24) and (25), we illustrated the potential distribution across space. Fig. 2(a) displays this distribution for specific parameters ($\alpha = 0, \sigma_{\text{r}} = 1, \theta = 0$) for different frequencies. At the lowest frequency, the potential gradient near the cell membrane is almost flat, indicating minimal current flow through the cell at this frequency. Additionally, the potential difference across the cell membrane is greatest at the lowest frequency. As the frequency increases, the potentials inside and outside the cell membrane converge. At the highest frequency, the gradient becomes uniform across the space, suggesting a continuous potential across the cell, which implies that the current flows through the cell at high frequency (as schematically hypothesized in Ehosioke *et al.* (2023) but with a different mechanism).

Fig. 2(a2) shows that the magnitude of the out-of-phase potential, $|\phi''^*|$, peaks at the middle frequency for the entire area. At this frequency, the disparity between the potentials inside and outside of the cell is also most pronounced, whereas it is minimal at both low and high frequencies.

Analysing ϕ'^* and ϕ''^* together, the cell behaves like a resistor at low frequencies, blocking current flow and showing no out-of-phase polarization. At high frequencies, the cell becomes 'invisible' to current flow, with no out-of-phase polarization detected. Such behaviours are reported in previous modelling studies of the cells (Asami 2006, 2007). However, at middle frequencies, the out-of-phase polarization is most significant, making the cell detectable by measuring ϕ''^*.

The behaviour of the cell at high frequencies differs from that of metals. In simulations, metals act as a bypass for the electric current at high frequencies (Izumoto 2023), whereas in our theoretical results, the cell appears as if it is not present, due to its similar conductivity to the surrounding water ($\sigma_{\text{r}} = 1$), unlike metals which are considered to have infinitely high conductivity. We consider this assumption ($\sigma_{\text{r}} = 1$) is reasonable because cells regulate osmotic pressure to reduce stress (Xiao & Zhou 2023), helping to maintain a stable salt concentration ratio between the inside and outside of the cell.

2.2.2 Potential and phase shift over frequency

Fig. 2(b) presents the analytical solution on the surface of the cell ($r' = 1$, outside of the cell) as a function of frequency, derived from eqs (21) and (22). We set parameters $\alpha = 0$ and $\sigma_{\text{r}} = 1$. The results display a typical polarization response; the real part of the potential (shown in Fig. 2b1) reaches its lower and upper limits asymptotically as the frequency decreases and increases, respectively. Meanwhile, the imaginary part of the potential and the phase shift (illustrated in Figs 2b2 and b3) each show a single peak.

To compare with experimental data, we focused on measurements where the current passes through the inside of the root. This includes single-root measurements (Ehosioke *et al.* 2023) and measurements in which one electrode is inserted into the stem and the other into the soil (Ozier-Lafontaine & Bajazet 2005; Cseresnyés *et al.* 2013; Peruzzo *et al.* 2021). In these latter cases, we assume that the measured phase shift is primarily caused by the plant rather than the soil, as its magnitude is similar to that of single-root measurements. The relevant data from previous studies are summarized in Table 2. Notably, the magnitude of the phase shift in our theory (Fig. 2b3) aligns with experimental findings.

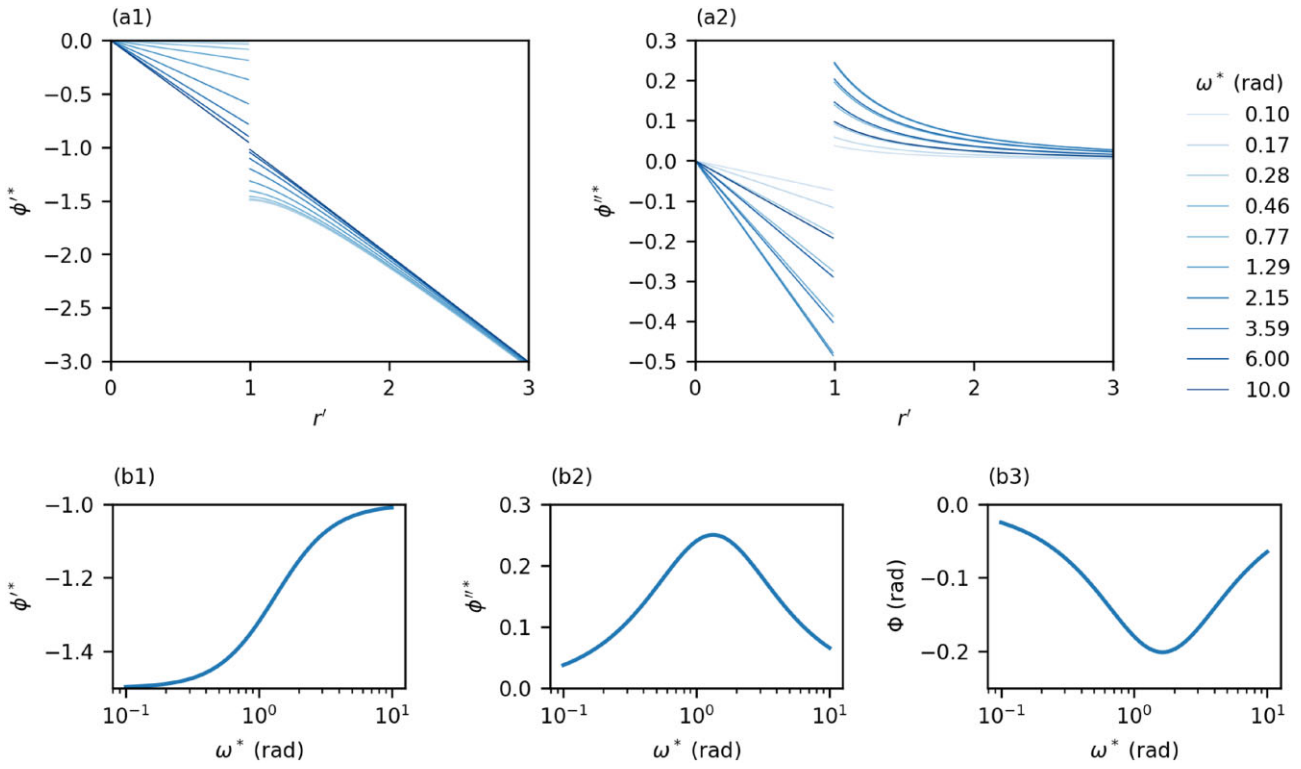

Figure 2. Theoretical results. Note that the non-dimensional frequency ω^* can be converted to ordinary frequency $f\,(s^{-1})$ by assuming the parameters discussed in theory section as $f = \omega/2\pi \approx 1.1 \times 10^6 \times \omega^* s^{-1}$. Also, non-dimensional distance r' is related to the dimensional distance r (μm) as $r = 20 \times r'$ μm. (a) Potentials over distance. (a1) Real part of the non-dimensional potential ϕ'^* and (a2) imaginary part of non-dimensional potential ϕ''^*. (b) The theoretical results at the surface of the cell. (b1) Real part of non-dimensional potential, ϕ'^*. (b2) Imaginary part of non-dimensional potential, ϕ''^*. (b3) Phase shift, Φ.

Table 2. List of studies that investigated the polarization of plant. We picked up the measurements with the largest absolute value of peak phase shift in each study. We excluded measurements where extracting data from the figure was difficult due to overlapping plots. Note that we exclude the studies that measured polarization of plant by putting all the electrodes in water or in soil, without directly touching plant, since we consider only the plant part and not the soil part.

	Ehosioke et al. (2023) (maize)	Ehosioke et al. (2023) (Brachypodium)	Cseresnyes et al. (2013)	Ozier-Lafontaine and Bajazet (2005)	Peruzzo et al. (2021)
Maximum $\lvert\Phi\rvert$ (rad)	0.5	0.62	0.64	0.65	0.58
Peak frequency (s^{-1})	4000	5000	1000	5700	over 8000
Electrodes' position	Root	Root	Stem and soil	Stem and soil	Stem and soil
Plant species	Maize	Brachypodium	Maize	Tomato	Pecan
Growth period	8 d after sowing	8 d after sowing	Between 10 and 27 d (averaged)	14 d after planting	From September to 26 April
Electrodes configuration	4 electrodes	4 electrodes	2 electrodes	2 electrodes	4 electrodes
Growth condition	Plastic tubes filled with fine and coarse sand	Plastic tubes filled with fine and coarse sand	Plastic cell containing Arenosol	Greenhouse	Hoop house

To convert non-dimensional frequency to ordinary dimensional frequency, we considered the thickness of the cell membrane ($l = 8$ nm) (Taiz & Zeiger 2002), its relative permittivity (set at 3, equivalent to $\varepsilon = 2.64 \times 10^{-11}\,\mathrm{F\,m^{-1}}$) (Stern & Feller 2003), and the conductivity of the water just outside the cell membrane. We calculated this conductivity based on ion concentrations (Taiz & Zeiger 2002) using PhreeqC software (Parkhurst & Appelo 2013), resulting in $\sigma_{out} = 0.9\,\mathrm{S\,m^{-1}}$. The cell's size, estimated from visual observations of Ehosioke *et al.* (2023), is about $R = 20$ μm.

The relationship between non-dimensional and dimensional frequencies is given by $\omega = l\sigma_{out}\omega^*/2R\varepsilon = 6.8 \times 10^6 \times \omega^*$. Hence, the ordinary frequency can be calculated as $f = \omega/2\pi \approx 1.1 \times 10^6 \times \omega^*$. Given that the peak frequency is near $\omega^* = 1$ (rad), these calculations suggest a peak frequency $f_c = 1.1 \times 10^6\,s^{-1}$, which does not align with previous experimental results. In the next section, we check if this discrepancy comes from the approximation of the parameters $\alpha = 0$ and $\sigma_r = 1$.

2.2.3 *Conductivity ratio σ_r and ion exchange parameter α^**

We derived the analytical solution for the peak frequency of the phase shift, $\omega^*_{C,\Phi}$, as shown in eq. (33). We plotted this relationship as a function of the conductivity ratio, σ_r, in Fig. 3(a1). The results indicate that a higher σ_r, which corresponds to higher internal conductivity of the cell, leads to an increased $\omega^*_{C,\Phi}$. Additionally, as the ion exchange parameter α^* increases, $\omega^*_{C,\Phi}$ becomes less influenced by σ_r below a certain σ_r (the higher the transfer, the higher contrast

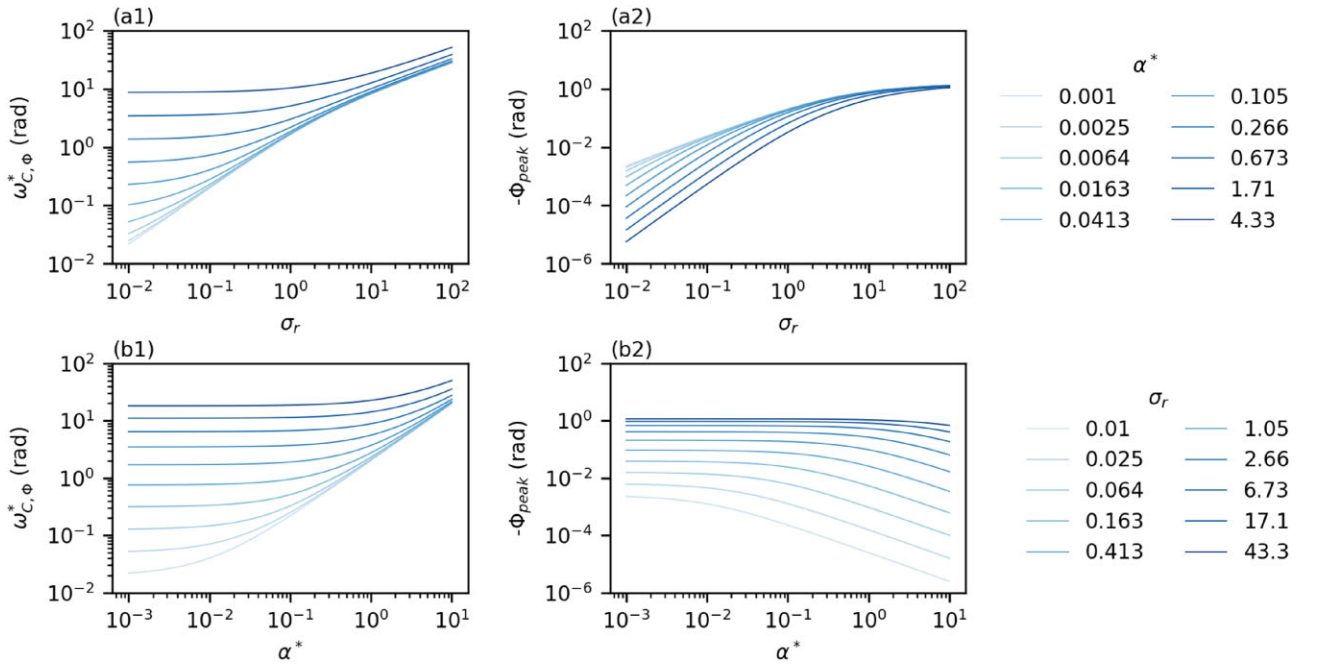

Figure 3. Theoretical results as a function of parameters representing the conductivity ratio between inside and outside the cell (σ_r and the ion exchange through the cell membrane (α^*). Note that the non-dimensional frequency ω^* can be converted to ordinary frequency $f\,(s^{-1})$ by assuming the parameters discussed in theory section as $f = \omega/2\pi \approx 1.1 \times 10^6 \times \omega^*$. (a) Dependency of peak frequency and peak phase shift on the ratio of conductivity between inside and outside the cell, σ_r. Lighter colour represents smaller α^*. (a1) The non-dimensional peak frequency, $\omega^*_{C,\Phi}$. (b2) Peak phase shift, Φ_{peak}. (b) Dependency of peak frequency and peak phase shift on the ion exchange across the cell membrane, α^*. Lighter colour represents smaller σ_r. (b1) The non-dimensional peak frequency, $\omega^*_{C,\Phi}$. (b2) Peak phase shift, Φ_{peak}.

needs to be to have an effect). This observation suggests that variations in ionic concentration between the inside and outside of the cell become less significant with increased ion exchange.

Furthermore, we examined the peak phase shift, Φ_{peak}, using eq. (35). We found that $|\Phi_{\text{peak}}|$ is larger for higher σ_r values (Fig. 3a2). This occurs since at low frequencies, the current does not pass through the cell, as opposed to the current path at high frequencies. The difference in current flow between these extremes approximately indicates the degree of polarization. Thus, a higher σ_r means the cell contributes more to the overall current flow at high frequencies, leading to a larger $|\Phi_{\text{peak}}|$.

We also analysed $\omega^*_{C,\Phi}$ as a function of α^*, shown in Fig. 3(b1), suggesting that $\omega^*_{C,\Phi}$ is higher for larger α^* values, likely because increased ion exchange reduces charge accumulation, allowing quicker establishment of polarization. Moreover, when σ_r is high, $\omega^*_{C,\Phi}$ shows reduced sensitivity to α^*, indicating that in such cases, the conductivity ratio, rather than ion exchange, becomes the limiting factor for polarization speed.

Lastly, we plotted Φ_{peak} against α^*, revealing that $|\Phi_{\text{peak}}|$ decreases as α^* increases due to reduced charge accumulation from more frequent ion exchanges (Fig. 3b2). When σ_r is high, $|\Phi_{\text{peak}}|$ is less sensitive to α^*, suggesting that ion exchange has only minor effect under large concentration within the cell. Although the value of α^* remains somewhat uncertain, the highest conductivity reported in the literature for ion channels is approximately $\alpha = 5\,\text{S}\,\text{m}^{-2}$ (Smith & Kerr 1987; Tyerman & Skerrett 1998). Note that value can change depending on the plant variety and that the activation of the ion channels and proton pump. This would then lead to values several orders of magnitude below ($10^{-3}\,\text{S}\,\text{m}^{-2}$) (Findlay *et al.* 1994). Based on calculations in Section 2.2.2., the ion exchange parameter is estimated to be $\alpha^* = 1.1 \times 10^{-6}$, indicating that the effect of ion exchange is likely negligible.

Finally, we check if we can match the analytical and experimental results of peak frequency and $|\Phi|$ by varying σ_r under $\alpha^* \approx 0$. According to the calculation in the Section 2.2.2., the analytical solution of the peak frequency at $\alpha^* = 0$ and $\sigma_r = 1$ ($f_c = 1.1 \times 10^6 s^{-1}$) needs to be more than 100 times lower to match the experimental results. Fig. 3(a1) shows that fixing α^* to the smallest value requires σ_r to be roughly 100 times smaller. However, Fig. 3(a2) shows that this also reduces $|\Phi|$ by roughly 100 times, resulting in $|\Phi| \approx 0.002$, which is much smaller than the experimental results shown in Table 2. Therefore, if we adjust σ_r to match the experimental peak frequency, $|\Phi|$ does not match, and vice versa.

From the above discussion, it is clear that the analytical solution in the simplified geometry does not fully explain the experimental results. Thus, we explored geometric effects through numerical simulations in the subsequent sections.

3 NUMERICAL SIMULATION

From our theoretical analysis, we determined that the peak frequency for a single cell within a large volume of water is too high with respect to experimental evidence. However, in actual roots, cells are densely packed within a small area inside the root (for example, see table 3 in Ehosioke *et al.* 2023), which requires further numerical investigation if we want to test different geometries, and cell density for instance. Additionally, we found that the effects of ion exchange through the cell membrane are minimal (see Fig. 3b2 for low values of α^*). Therefore, in our simulations, we focus on the impact of geometric factors (cell size, shape and density) without considering ion exchange. The simulations are implemented

with the open-source computational-fluid-dynamic software OpenFOAM (https://openfoam.org/).

3.1 Governing equations

When attempting to apply the same boundary conditions on both sides of the membrane as those in the analytical equations (eqs 6 and 7) after converting from time domain to frequency domain, the numerical solutions were unstable and failed to converge. To address this issue, we simplified the model by reducing the number of independent equations to two, as outlined below. Eqs (6) and (7) yield:

$$\frac{\partial \phi_{\text{in}}}{\partial t} = \frac{\partial \phi_{\text{out}}}{\partial t} - \frac{l\sigma_{\text{out}}}{2\varepsilon}\left(\frac{\partial \phi_{\text{out}}}{\partial r_{\text{out}}} + \frac{\sigma_{\text{in}}}{\sigma_{\text{out}}}\frac{\partial \phi_{\text{in}}}{\partial r_{\text{in}}}\right). \tag{37}$$

After transform, the real part and imaginary part of potentials are obtained as:

$$\phi'_{\text{in}} = \phi'_{\text{out}} - \frac{l\sigma_{\text{out}}}{2\varepsilon\omega}\left(\frac{\partial \phi''_{\text{out}}}{\partial r_{\text{out}}} + \frac{\sigma_{\text{in}}}{\sigma_{\text{out}}}\frac{\partial \phi''_{\text{in}}}{\partial r_{\text{in}}}\right), \tag{38}$$

$$\phi''_{\text{out}} = \phi''_{\text{in}} + \frac{l\sigma_{\text{out}}}{2\varepsilon\omega}\left(\frac{\partial \phi'_{\text{out}}}{\partial r_{\text{out}}} + \frac{\sigma_{\text{in}}}{\sigma_{\text{out}}}\frac{\partial \phi'_{\text{in}}}{\partial r_{\text{in}}}\right). \tag{39}$$

Note that, in the membrane inner boundary for analytical case (eqs 6 and 7), when $\alpha = 0$ and $\omega = 0$, we obtain the conditions:

$$\frac{\partial \phi_{\text{in}}}{\partial r_{\text{in}}} = \frac{\partial \phi_{\text{out}}}{\partial r_{\text{out}}} = 0. \tag{40}$$

On the other hand, when $\omega = 0$, the above governing equations for the numerical simulations (eqs 39 and 38) only give:

$$\frac{\sigma_{\text{in}}}{\sigma_{\text{out}}}\frac{\partial \phi'_{\text{in}}}{\partial r_{\text{in}}} = -\frac{\partial \phi'_{\text{out}}}{\partial r_{\text{out}}}. \tag{41}$$

For the imaginary part, we presumed $\phi''_{\text{in}} = \phi''_{\text{out}} \approx 0$ for $\omega = 0$ given the conceptual view. Thus, the numerical equation for the real part of potential (eq. 38) should be modified. We separated the real part into the externally applied potential and induced potential as:

$$\phi'_{\text{out}} = \phi_{\text{ex}} + \phi'_{\text{ind}}, \tag{42}$$

where ϕ_{ex} is the externally applied potential and ϕ'_{ind} is the real part of induced potential. Since cell membrane does not pass through the in-phase component of the potential, ϕ_{ex} satisfies

$$\frac{\partial \phi_{\text{ex}}}{\partial r_{\text{out}}} = 0. \tag{43}$$

From the conceptual view, $\phi_{\text{ind}} = 0$ for $\omega = 0$. Thus, by taking the derivative of eq. (42) with respect to r_{out}, we obtained $\frac{\partial \phi_{\text{out}}}{\partial r_{\text{out}}} = 0$. This is now consistent with the analytical case, eq. (40). The potentials, ϕ_{ex}, ϕ'_{ind}, ϕ''_{in}, ϕ'_{out} and ϕ''_{out}, satisfy Laplace's equation:

$$\nabla^2 \phi = 0. \tag{44}$$

From eqs (38), (39) and (42), potentials on the cell membrane can be written as:

$$\phi'_{\text{in}} = \phi_{\text{ex}} + \phi'_{\text{ind}} - \frac{l\sigma_{\text{out}}}{2\varepsilon\omega}\left(\frac{\partial \phi''_{\text{out}}}{\partial r_{\text{out}}} + \frac{\sigma_{\text{in}}}{\sigma_{\text{out}}}\frac{\partial \phi''_{\text{in}}}{\partial r_{\text{in}}}\right), \tag{45}$$

$$\phi''_{\text{out}} = \phi''_{\text{in}} + \frac{l\sigma_{\text{out}}}{2\varepsilon\omega}\left(\frac{\partial \phi'_{\text{ind}}}{\partial r_{\text{out}}} + \frac{\sigma_{\text{in}}}{\sigma_{\text{out}}}\frac{\partial \phi'_{\text{in}}}{\partial r_{\text{in}}}\right). \tag{46}$$

Above equations were transformed to non-dimensional form as below (summary in in Table 3). For the potentials in the field:

$$\nabla^{*2}\phi^* = 0, \tag{47}$$

$$\phi'^{*}_{\text{out}} = \phi^*_{\text{ex}} + \phi'^{*}_{\text{ind}}, \tag{48}$$

where all the potentials denoted by $*$ are normalized by characteristic potential ϕ_0, and ∇ is taken in the non-dimensional space. On the surface of cell, the in-phase component of electrical current perpendicular to the cell surface, J_{ex}, does not pass through the membrane. Thus, ϕ^*_{ex} satisfies

$$J_{\text{ex}} = \frac{\partial \phi^*_{\text{ex}}}{\partial r'_{\text{out}}} = 0 \tag{49}$$

with $r'_{\text{out}} = r_{\text{out}}/L$, where L is characteristic length. On the cell membrane, ϕ'^{*}_{in} and ϕ''^{*}_{out} are given by

$$\phi'^{*}_{\text{in}} = \phi^*_{\text{ex}} + \phi'^{*}_{\text{ind}} - \frac{1}{\omega^*}\left(\frac{\partial \phi''^{*}_{\text{out}}}{\partial r'_{\text{out}}} + \sigma_r \frac{\partial \phi''^{*}_{\text{in}}}{\partial r'_{\text{in}}}\right), \tag{50}$$

$$\phi''^{*}_{\text{out}} = \phi''^{*}_{\text{in}} + \frac{1}{\omega^*}\left(\frac{\partial \phi'^{*}_{\text{ind}}}{\partial r'_{\text{out}}} + \sigma_r \frac{\partial \phi'^{*}_{\text{in}}}{\partial r'_{\text{in}}}\right), \tag{51}$$

where $\omega^* = 2\varepsilon\omega L/l\sigma_{\text{out}}$ is non-dimensional angular frequency and $\sigma_{\text{r}} = \sigma_{\text{in}}/\sigma_{\text{out}}$ is the relative conductivity inside of the cell relative to that of outside. To satisfy the membrane inner boundary conditions specified in eqs (50) and (51), these values were updated iteratively following the equation and stop when the 'initial residual' value in the Laplacian solver in OpenFOAM reaches below 2×10^{-6}, except for Scenario 3 (10^{-5}) and Scenario 4 (2×10^{-4}) shown in the next section:

$$\phi'^{*}_{\text{in},n+1} = \phi'^{*}_{\text{in},n} - \delta s\left(\phi'^{*}_{\text{in},n} - \left(\phi^*_{\text{ex},n} + \phi'^{*}_{\text{ind},n} - \frac{1}{\omega^*}\left(\frac{\partial \phi''^{*}_{\text{out},n}}{\partial r'_{\text{out}}} + \sigma_r \frac{\partial \phi''^{*}_{\text{in},n}}{\partial r'_{\text{in}}}\right)\right)\right) \tag{52}$$

$$\phi''^{*}_{\text{in},n+1} = \phi''^{*}_{\text{in},n} - \delta s\left(\phi''^{*}_{\text{in},n} - \left(\phi''^{*}_{\text{out},n} - \frac{1}{\omega^*}\left(\frac{\partial \phi'^{*}_{\text{ind},n}}{\partial r'_{\text{out}}} + \sigma_r \frac{\partial \phi'^{*}_{\text{in},n}}{\partial r'_{\text{in}}}\right)\right)\right) \tag{53}$$

$$\phi'^{*}_{\text{ind},n+1} = \phi'^{*}_{\text{ind},n} - \delta s\left(\phi'^{*}_{\text{ind},n} - \left(\phi^*_{\text{in},n} - \phi'_{\text{ex},n} + \frac{1}{\omega^*}\left(\frac{\partial \phi''^{*}_{\text{out},n}}{\partial r'_{\text{out}}} + \sigma_r \frac{\partial \phi''^{*}_{\text{in},n}}{\partial r'_{\text{in}}}\right)\right)\right) \tag{54}$$

$$\phi''^{*}_{\text{out},n+1} = \phi''^{*}_{\text{out},n} - \delta s\left(\phi''^{*}_{\text{out},n} - \left(\phi''^{*}_{\text{in},n} + \frac{1}{\omega^*}\left(\frac{\partial \phi'^{*}_{\text{ind},n}}{\partial r'_{\text{out}}} + \sigma_r \frac{\partial \phi'^{*}_{\text{in},n}}{\partial r'_{\text{in}}}\right)\right)\right) \tag{55}$$

where n is the iterative index, δs is a factor for the numerical convergence to satisfy the inner boundary condition, which was found to be between 5×10^{-5} and 10^{-2} by trial and error, with lower and higher values for lower and higher frequencies, respectively.

In the simulation, we did not account for charge distribution, which can vary significantly within a nanometer scale near the cell membrane. To accurately model charge distribution, a numerical simulation would require an extremely fine mesh. However, the potential distribution resulting from this charge accumulation changes more gradually over space. Consequently, by omitting charge distribution from our equations, we avoid the need for such fine-scale resolution. This allowed us to focus more effectively on studying geometric factors at the micrometer scale, which is a significant advantage of our approach in terms of computation times.

3.2 Simulation domain

Our simulation grid included at least 200 mesh elements in the x-direction, and at least 50 mesh elements in the y and z directions, totalling more than 5×10^5 meshes. The simulation domain was configured as a rectangular prism (see Fig. 4) defined by the coordinates $x \in [-a_d/2, a_d/2]$, $y \in [-b_d/2, b_d/2]$, and $z \in [-b_d/2, b_d/2]$. Within this domain, we modelled a cell as a rectangular prism sized (a_c, b_c, b_c), as depicted in Fig. 4(a). Note that both the y and the z dimensions for the domain and the cell are

Table 3. The list of parameters used in the governing equations of the simulations, and the conversion from dimensional variables to dimensionless variables.

	Potential	Frequency	Coordinate	Conductivity	Permittivity Membrane thickness Characteristic length Characteristic potential
Dimensional	$\phi_{ex}, \phi'_{ind}, \phi''_{in}, \phi'_{out}, \phi''_{out}$	ω	r_{in}, r_{out}	$\sigma_{in}, \sigma_{out}$	$\varepsilon, l, L, \phi_0$
Dimensionless	$\phi^*_{ex}, \phi'^*_{ind}, \phi''^*_{in}, \phi'^*_{out}, \phi''^*_{out}$	ω^*	r'_{in}, r'_{out}	σ_r	–
Conversion from dimensional to dimensionless	Divide by ϕ_0	$\omega^* = 2\varepsilon\omega L/l\sigma_{out}$	Divide by L	$\sigma_r = \sigma_{in}/\sigma_{out}$	–

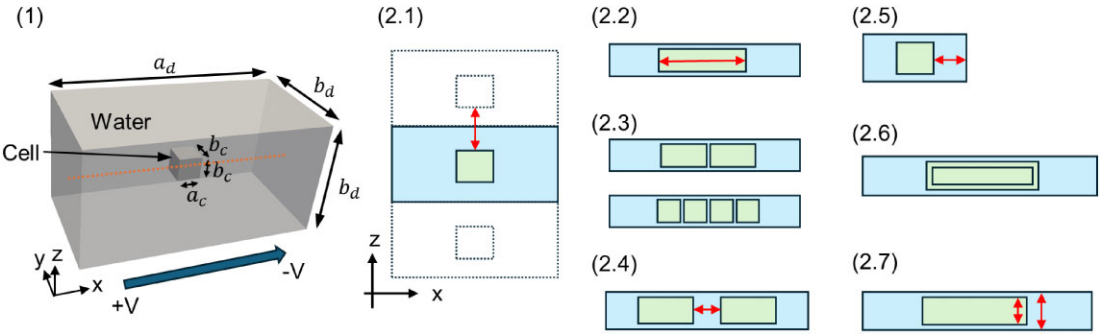

Figure 4. The simulation setting. (a) The simulation domain, with the cell surrounded by water. The origin (0,0,0) is set at the centre of the domain. The orange line represents the sampling line ($y = z = 0$) of potential for the plot in Fig. 6. (b) The simulation scenarios. (b.1) Scenario 1: distance to the nearby cell perpendicular to the electric current. (b.2) Scenario 2: length of the cell. (b.3) Scenario 3: cell density. (b.4) Scenario 4: distance to the nearby cell horizontal to the electric current. (b.5) Scenario 5: relative cell volume. (b.6) Scenario 6: double membrane cell. (b.7) Scenario 7: thickness of the cell.

always equal. For all simulations, we assumed a conductivity ratio between the water and the cell, $\sigma_r = 1$, to primarily explore geometric effects. The boundary conditions were set as $\phi^*_{ex} = \{1, -1\}$ (externally imposed potential) at $x = \{-a_c/2, a_c/2\}$ and $\partial\phi'^*_{out}/\partial x = \partial\phi''^*_{out}/\partial x = 0$. For the other boundaries at $y = \{-b_c/2, b_c/2\}$ and $z = \{-b_c/2, b_c/2\}$, we applied $\partial\phi^*_{ex}/\partial y = \partial\phi'^*_{out}/\partial y = \partial\phi''^*_{out}/\partial y = 0$ and $\partial\phi^*_{ex}/\partial z = \partial\phi'^*_{out}/\partial z = \partial\phi''^*_{out}/\partial z = 0$, respectively. The cell membrane was modelled using eqs (50) and (51).

After running the simulations, the real part of the potential outside the cell was calculated by eq. (48). To standardize the potentials, we normalized all potentials by ϕ'^*_{out} at the boundary $x = \{-a_c/2, a_c/2\}$ for each simulation, ensuring that ϕ'^*_{out} at these boundaries was always 1 and -1, respectively.

We varied the size of the domain, the size of the cell and the number of cells to examine the impact of geometry. The goal is to develop a simple model or identify a fundamental mechanism that can reasonably explain the observed IP responses, rather than reproducing the varied experimental conditions of previous studies. In reality, plant root anatomy is far more complex, including features such as symplastic pathways, ion pumps and dead cells (Taiz & Zeiger 2002). We configured several scenarios as follows, summarized in Fig. 4(b) and Table 4:

Scenario 1: distance to nearby cell perpendicular to electric current (Fig. 4b1). In this scenario, cells were aligned in parallel, and we simulated only one cell due to symmetry. The cell dimensions were set as $a_c = b_c = 1$ and $a_d = 10$, with varying distances between cells ($b_d \in \{3, 1.75, 1.125\}$). Since all dimensions were non-dimensional, the cubic cell was defined as the characteristic length, which served as a reference for all measurements in our simulations. We also checked simulations by refining the mesh in the x-direction and ensuring that the simulation results remained consistent.

Scenario 2: length of the cell (Fig. 4b2). Here, we maintained the smallest distance between cells from Scenario 1 ($b_d = 1.125$), with the domain length $a_d = 10$ and cell height and depth $b_c = 1$. We explored variations in the cell's length perpendicular to the electric current with lengths $a_c \in \{3.125, 6.25\}$.

Scenario 3: cell density (Fig. 4b3). The domain size was consistent with Scenario 2 ($a_d = 10$ and $b_d = 1.125$). We increased cell density by splitting the longest cell from Scenario 2 ($b_c = 1$, $a_c = 6.25$) into 2 or 4 parts. After splitting, the distances between cells were 0.3 for all cases, with new cell lengths of $a_c = 3.05$ for splitting into 2, and $a_c = 1.41$ and 1.49 for the middle and edge cells, respectively, when splitting into 4.

Scenario 4: distance to nearby cell horizontal to electric current (Fig. 4b4). The domain size remained as in Scenario 2 ($a_d = 10$ and $b_d = 1.125$). We placed two cells of size $a_c = 3.125$ and $b_c = 1$, with a distance of 4.05 between them, significantly more than the 0.3 used in Scenario 3.

Scenario 5: relative cell volume (Fig. 4b5). To alter the relative volume of the cell within the domain, we reduced the domain size to $a_d = 1.6$, much smaller than $a_d = 10$ used in other scenarios. The cell dimensions remained the same as in Scenario 1 ($a_c = b_c = 1$), with the same distance to the nearby cell as in Scenario 2 ($b_d = 1.125$).

Scenario 6: double membrane cell (Fig. 4b6). We explored cells with double membranes, representing cells packed within another membrane-bound volume. This scenario mimics two membranes in plant cells; plasma membrane and middle lamella. Thus, this represents a case where the DC electric current flows through the middle lamella rather than the secondary wall. The domain and outer membrane dimensions were the same as in Scenario 2 ($a_d = 10$, $b_d = 1.125$), with the outer membrane dimensions $b_c = 1$ and $a_c = 6.25$, enclosing a cell sized $b_{c2} = 0.75$ and $a_{c2} = 5.75$.

Table 4. List of geometric parameters used in simulation. Scenario 1: distance to the nearby cell perpendicular to electric current. Scenario 2: length of the cell. Scenario 3: cell density. Scenario 4: distance to the nearby cell horizontal to electric current. Scenario 5: relative cell volume. Scenario 6: double membrane cell. Scenario 7: thickness of the cell.

	Scenario 1	Scenario 2	Scenario 3	Scenario 4	Scenario 5	Scenario 6	Scenario 7
a_d	10	10	10	10	1.6	10	10
b_d	{1.125, 1.75, 3}	1.125	1.125	1.125	1.125	1.125	0.5625
a_c	1	{3.125, 6.25}	{3.05 (2 cells), 1.41 and 1.49 (4 cells)}	3.05	1	1 (outer), 0.75 (inner)	6.25
b_c	1	1	1	1	1	1 (outer), 0.75 (inner)	0.5
Note	–	–	2 and 4 cells	2 cells Cell distance 4.05	–	double membrane	–

Scenario 7: thickness of the cell (Fig. 4b7). This scenario investigated the effects of a cell becoming thinner without altering its length. The domain and cell lengths were consistent with Scenario 2 ($a_d = 10$ and $a_c = 6.25$), but the cross-sectional area of both the domain and the cell were reduced, setting $b_d = 0.5625$ and $b_c = 0.5$. Note that in this case $sigma_r$ could take different values but here we kept them constant.

Each scenario focused on different geometric aspects, allowing us to assess how variations in cell arrangement and dimensions influence the polarization.

3.3 Simulation results

3.3.1 Scenario 1: distance to the nearby cell perpendicular to the electric current

This scenario explored how electrical signals are affected by changes in the distance to adjacent cells perpendicular to the electric field. Figs 5(a1)–(a3) displays the real part of the potential (ϕ'^*), the imaginary part of the potential (ϕ''^*) and the phase shift (Φ) at the cell surface on the water side at $(x, y, z) = (-1, 0, 0)$. The influence of distance to neighbouring cells on the potential values is highly nonlinear; notably, in the closest case ($a_d = 1.125$), the absolute values of the potentials are significantly larger than in other cases in the entire frequency for ϕ'^* and at low frequecies for ϕ''^*. This is due to the narrower current path outside the cell, which possesses higher resistance, thereby resulting in a greater potential difference across this path. This observation aligns with previous simulations that studied the polarization of metal grains in narrow channels Izumoto (2023). This observation also highlights the importance of cell spacing in actual plant roots, where cells are densely packed. Additionally, direct contact between cells and the symplastic pathway, which connects them, may play a significant role, as discussed in Peruzzo *et al.* (2021).

Interestingly, while the absolute values of ϕ'^* and ϕ''^* can double when the nearby cell is closer, the phase shift (Φ), which is calculated as $\arctan(\phi''^*/\phi'^*)$, only changes by about 10 per cent. This indicates that despite the substantial changes in ϕ'^* and ϕ''^*, these changes largely cancel out in the phase shift calculation.

The spatial distribution of the potential outside the cell is illustrated in Fig. 6. At the lowest frequency, the gradient of ϕ' at the cell surface is nearly zero, implying no current flow through the cell (as shown in the top row of Fig. 6a and in Fig. 6b). At the highest frequency, the potential distribution behaves as if the cell were invisible, consistent with the theoretical predictions in Section 2.2.1 and demonstrated in Fig. 2.

Across all cases, the magnitude of the imaginary part of the potential, $|\phi''|$, is greatest on the cell surface. As the distance to nearby cells increases, $|\phi''|$ declines more sharply in space. Conversely, as cells are positioned closer together, the decline in $|\phi''^*|$ becomes less steep, which ties into discussions on coupling polarization in later sections.

3.3.2 Scenario 2: length of the cell

In this scenario, we adjusted the length of the cell horizontally relative to the electric current direction. Measurements were taken on the cell surface at $(x, y, z) = (-a_c/2, 0, 0)$ on the water side. The results demonstrated that both the absolute values of the real potential ($|\phi'^*|$) and the imaginary potential ($|\phi''^*|$) increased gradually with the cell length (Figs 5b1 and b2). This increase occurs because a longer cell experiences a greater potential difference across its length. However, the magnitude of the peak phase shift (Φ) remained relatively unchanged (Fig. 5b3), suggesting that the changes in ϕ'^* and ϕ''^* are proportional and effectively cancel each other out when calculating Φ, regardless of the cell's length.

Interestingly, the peak frequency decreases for longer cells. For instance, if the cell's length is increased sixfold, the peak frequency decreases by about 1/100th. This trend is more pronounced than what the analytical solution predicted (eq. 23), which suggested that peak frequency is inversely proportional to the sphere's radius. This discrepancy arises because the analytical model assumed a spherical shape and infinitely distant boundaries, whereas in the simulation, other cells are quite close. This difference highlights that the proximity of neighbouring cells enhances the sensitivity to the size of the cell in our simulations.

3.3.3 Scenario 3: cell density

In Scenario 3, a long cell is segmented into smaller sections to increase the cell density. Measurements are taken from the centre of the left surface of the most leftward cell (the cell at the smallest x-value), with $y = z = 0$. Notably, even after splitting the cells, the response remained largely unchanged (Figs 5c1–c3). This key finding demonstrates that even smaller cells can polarize collectively under certain geometric constraints. This phenomenon indicates that there is coupling during polarization; the induced polarization in one cell creates a potential that affects nearby cells when they are close together.

This strong coupling effect is likely influenced by the distance to the nearest cell perpendicular to the electric current, as explored in Scenario 1. When cells are spaced widely apart, with no nearby cells, the potential induced by one cell's surface tends toward zero at a distance from the cell (Fig. 6). Conversely, under geometric constraints, such as when cells are close together, the potential does not reach zero even at a distance. This persistent potential under constrained conditions would significantly enhance the coupling between cells.

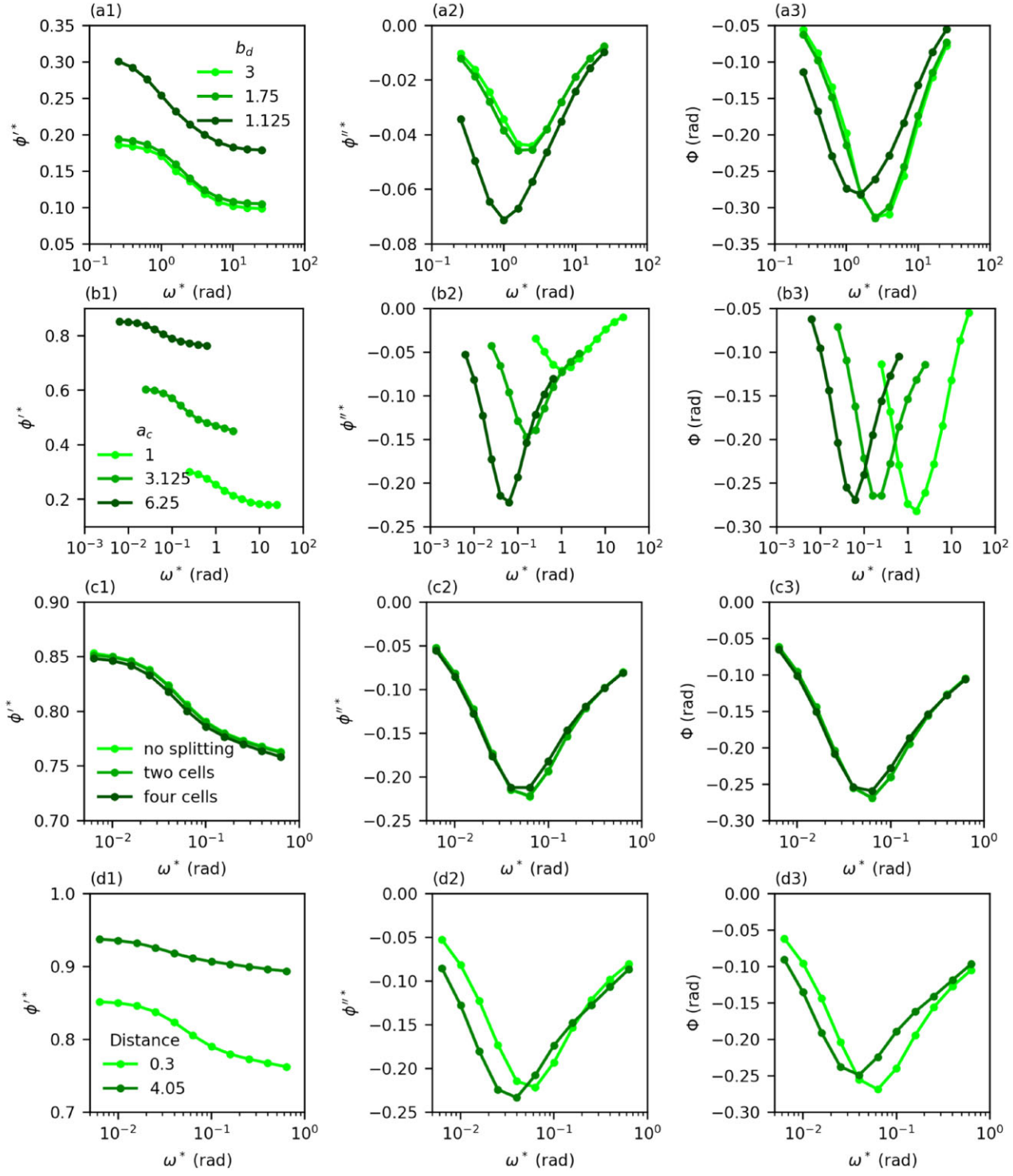

Figure 5. Results of simulations from Scenario 1 to Scenario 4. Real part of non-dimensional potential, ϕ'^* (left column). Imaginary part of non-dimensional potential, ϕ''^* (middle column). Phase shift, Φ (right column). All the values are sampled on the surface of the cell. Each row corresponds to each scenario. (a1–a3) Scenario 1: distance to the nearby cell perpendicular to the electric current. (b1–b3) Scenario 2: length of the cell. (c1–c3) Scenario 3: cell density. (d1–d3) Scenario 4: distance to the nearby cell horizontal to the electric current.

3.3.4 Scenario 4: distance to the nearby cell horizontal to the electric current

In this analysis, we adjusted the distance to the nearby cell positioned horizontally relative to the electric current. Measurements were taken from the centre of the left surface of the cell at the smallest x-value, with $y = z = 0$. Despite varying the distance by up to tenfold, the responses show minimal change: ϕ'^* increase by only about 10 to 20 per cent, and the peak values of $|\phi''^*|$ and $|\Phi^*|$ alter by just around 10 per cent (Figs 5d1–d3). The observed reduction in peak

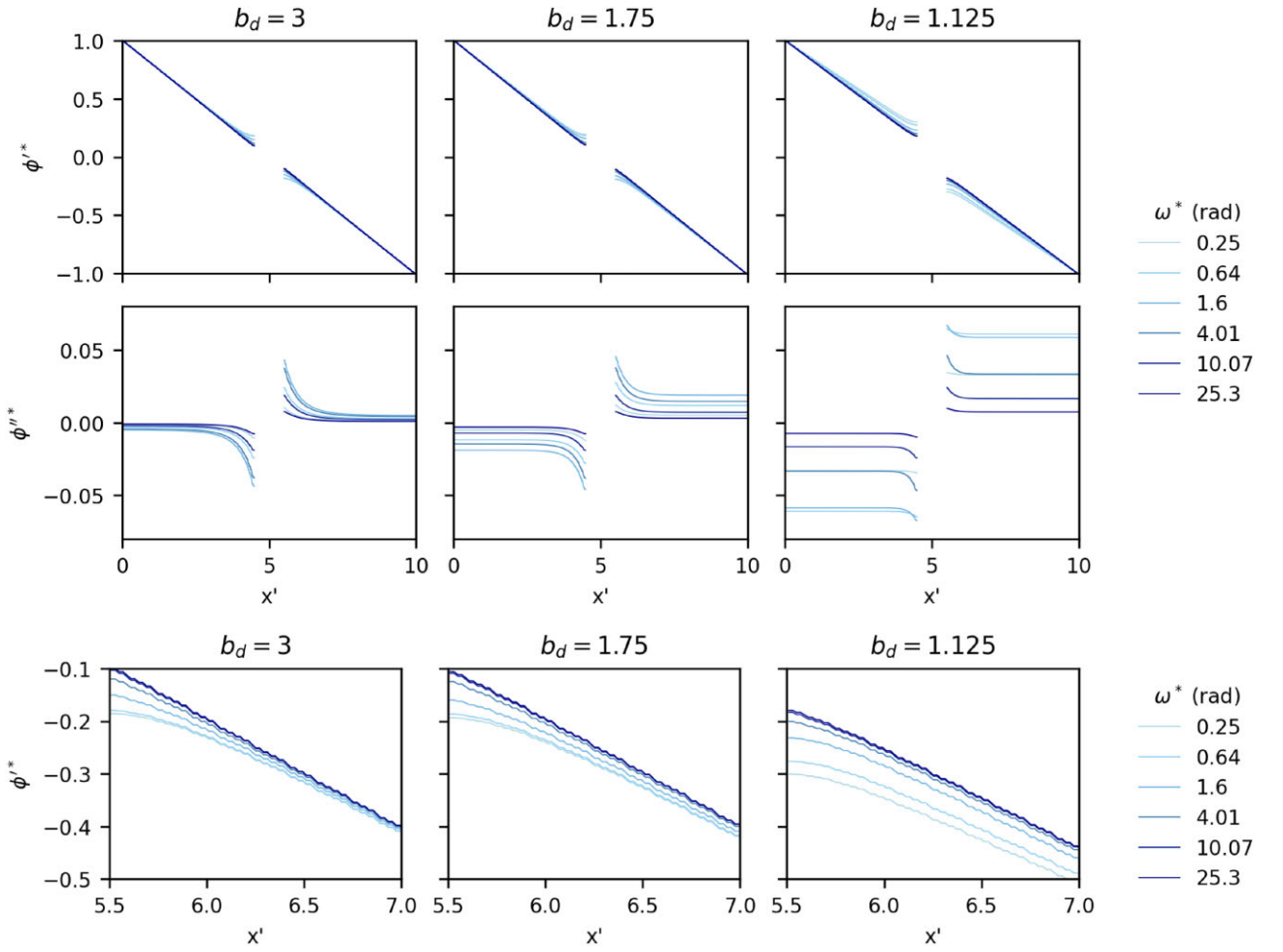

Figure 6. Results of Scenario 1 in space ($y = z = 0$). Lighter colour represents lower frequency. See Fig. 4(1) for the sampling line. (a) The real part and imaginary part of potential distribution (top row and bottom row, respectively) at $b_d = 3, 1.75, 1.125$ (left, middle and right column, respectively) at different frequency. (b) The close up of real part of potential distribution close to the cell at $b_d = 3, 1.75, 1.125$ (left, middle and right column, respectively) at different frequency. The wiggles are the numerical effect due to the discretization of the space.

frequency at longer distances can be attributed to longer relaxation times, suggesting that the effective length scale is greater when cells are more widely spaced.

These results—relatively consistent values of ϕ'^*, ϕ''^* and Φ with a slightly lower peak frequency in larger spaces—indicate that the cells remain coupled for polarization even when separated by greater distances. Similar to the findings in Scenario 3, this persistence in coupling is influenced by geometric constraints, which continue to facilitate interactions between cells regardless of their separation.

3.3.5 Scenario 5: relative cell volume

This scenario explored the effects of changing the relative volume of the cell compared to the entire measurement domain. Measurements were taken on the surface of the cell at $(x, y, z) = (-1, 0, 0)$. That potentials are larger when the cell occupies a larger space because a larger electrical field is applied (Figs 7a1 and a2). However, the phase shift (Φ) remains almost constant (Fig. 7a3). This consistency in Φ occurs despite the increases in ϕ'^* and ϕ''^* because these values effectively cancel each other out in the calculation of Φ.

Importantly, the stability of Φ across changes in cell volume confirms that the trends observed in Φ in other scenarios are not influenced by the relative volume of the cell within the domain, but rather by other factors investigated in those scenarios.

3.3.6 Scenario 6: double membrane cell

In the scenario with a double membrane, we modelled a situation where a cell is enclosed by an additional membrane. Measurements were taken on the cell surface at $(x, y, z) = (-1, 0, 0)$. Unlike other scenarios, significant changes are observed in the shape of the curve for the imaginary part of the potential (ϕ''^*) and the phase shift (Φ), with two distinct peak frequencies appearing (Figs 7b2 and b3). One peak occurs at a slightly lower frequency than what is typical for a single membrane cell, and the other at a frequency about ten times higher. This indicates the presence of two distinct timescales of polarization. The first is similar to the polarization timescale of the outer membrane, akin to that observed in the single membrane scenario. The second, about ten times shorter, likely involves a much smaller scale of polarization, potentially within the space between the inner and outer cell membranes.

Additionally, the peak magnitude of the phase shift ($|\Phi|$) in this double membrane case is approximately 65 per cent of what is observed in the single cell case at both peaks (Fig. 7b3). This can be explained by considering the distribution of charges involved in

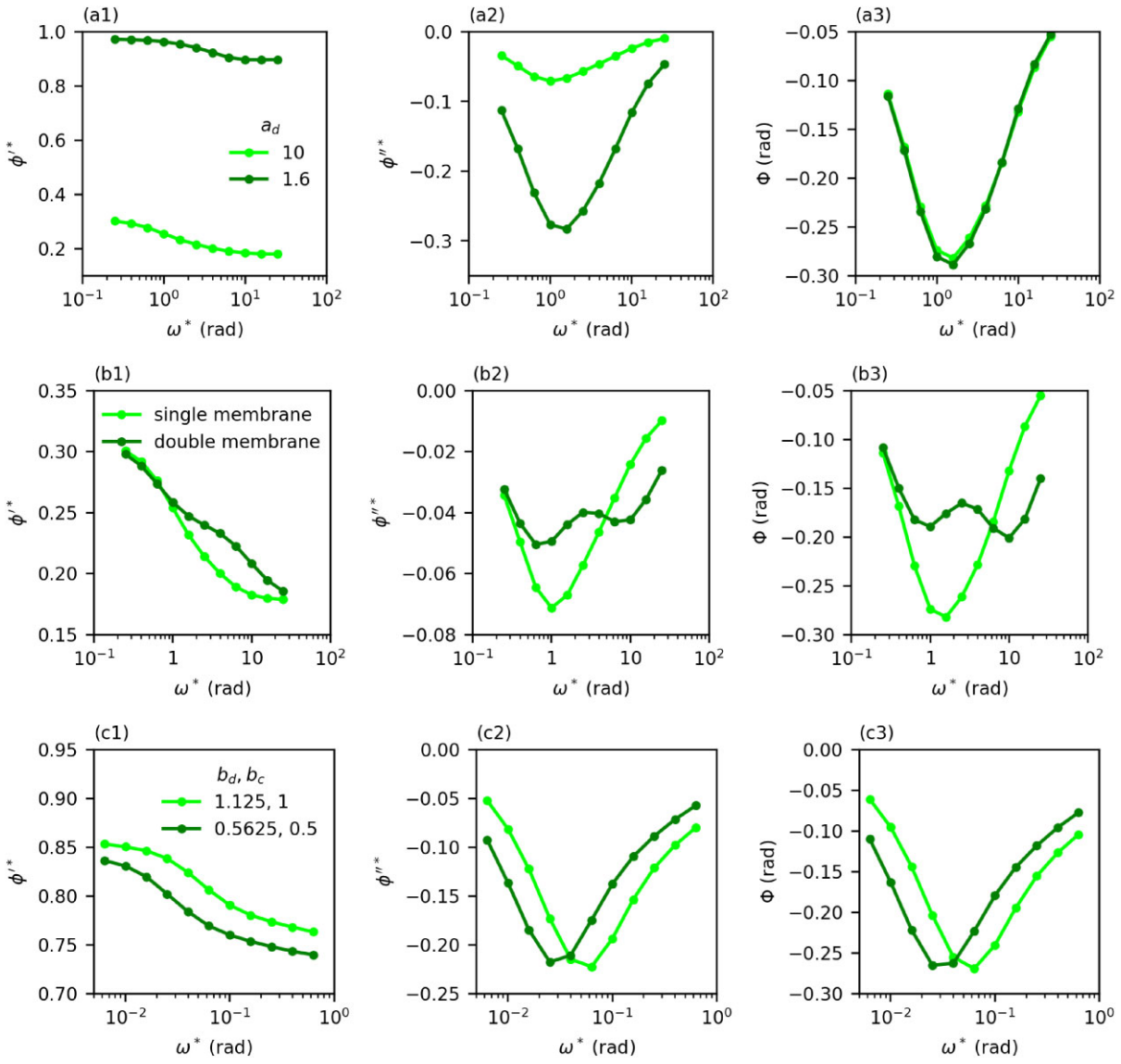

Figure 7. Results of simulations from Scenario 5 to Scenario 7. Real part of non-dimensional potential, ϕ'^* (left column). Imaginary part of non-dimensional potential, ϕ''^* (middle column). Phase shift, Φ (right column). The values are sampled on cell surface. Each row corresponds to each scenario. (a1–a3) Scenario 5: relative cell volume. (b1–b3) Scenario 6: double membrane cell. The values are sampled on the surface of the outer membrane. (c1–c3) Scenario 7: thickness of the cell.

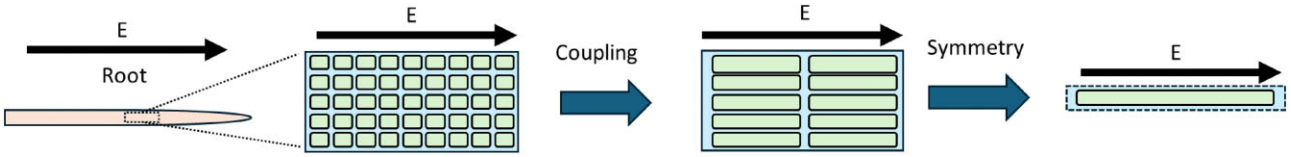

Figure 8. Schematics showing how the root cells are simplified to compare the simulation results with experimental results in previous studies.

the polarization process. In a double membrane cell, the charges are divided between two spaces: inside the inner membrane and the interstitial space between the inner and outer membranes. As each space contributes to different peak frequencies, the amount of charge involved in each polarization event is less than in the single membrane case, where the entire cell's charge contributes to a single peak. Consequently, each peak $|\Phi|$ in the double membrane scenario is smaller than in the single membrane case.

3.3.7 Scenario 7: thickness of the cell

This scenario examined the effects of a cell having a thinner cross-sectional area. Measurements were taken on the cell surface at $(x, y, z) = (-a_c/2, 0, 0)$. The overall shapes of the curves for the imaginary part of the potential (ϕ''^*) and the phase shift (Φ) are nearly identical whether the cell is thinner or thicker (Figs 7c2 and c3). However, the peak frequency for the thinner cell, which has a cross-sectional area four times smaller than that of the thicker cell, is half that of the thicker cell.

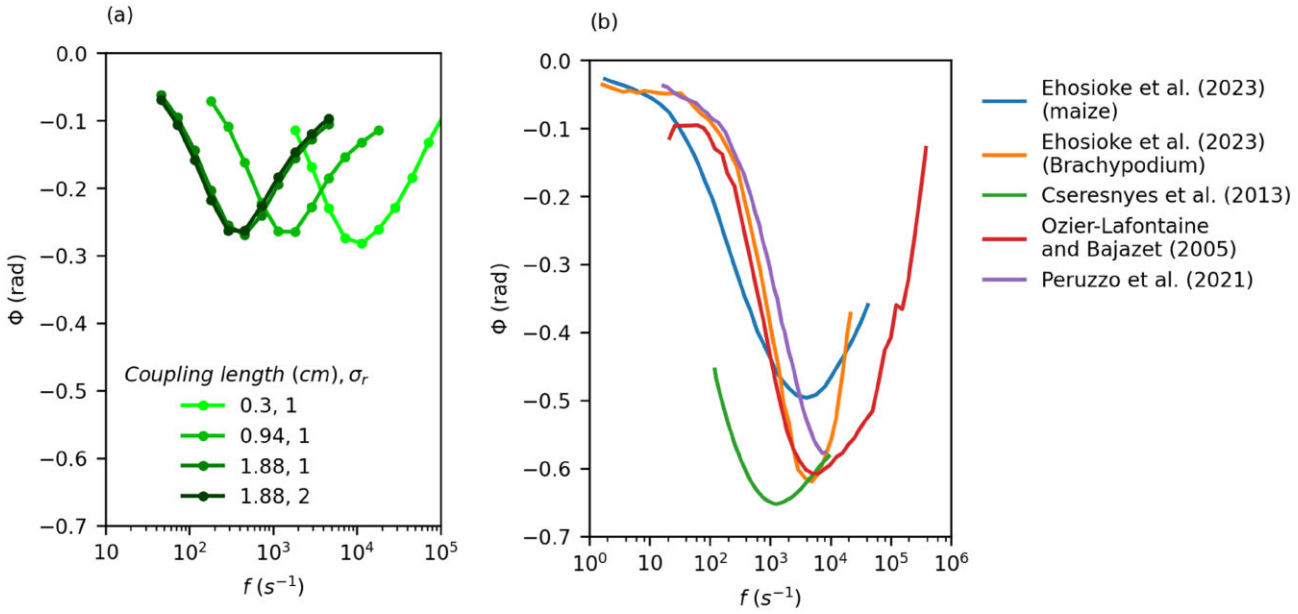

Figure 9. Dimensional results of the simulations. (a) Phase shift at the surface of the cell of Scenario 2 converted to dimensional frequency (simulations with $\sigma_r = 1$), as well as the new simulation result of $\sigma_r = 2$ using the same geometric configuration as the longest cell in Scenario 2. (b) The phase shift observed in previous studies. We picked up the measurements with the largest absolute value of peak phase shift in each study, as shown in Table 1.

Notably, when comparing Φ or ϕ''^* at the same frequency across different cell thicknesses, significant differences emerge, except near the peak frequency. This variance indicates that measurements taken at a single frequency can be highly sensitive to the thickness of the cell. Previous studies, such as Cseresnyés *et al.* (2018), have utilized single frequency measurements in applications to crop sciences. Our simulations suggest that the interpretations of such studies should take into account the cross-sectional area of the cell to ensure accuracy and relevance of the results.

3.4 Short summary of main results

Here, we summarize the main findings from each scenario in the simulations:

Scenario 1: When a nearby cell perpendicular to the electric current is closer, the potential decreases less steeply in space, indicating that proximity between cell membranes as modelled here influences the electric field.

Scenario 2: Lengthening the cell results in a decrease in peak frequency, though the overall magnitude of the phase shift remains relatively constant, suggesting that cell length affects the frequency of peak polarization but not its intensity.

Scenario 3: Increasing the cell density by splitting a long cell into several pieces does not significantly alter the response, indicating that the polarization across the split cells is coupled, showing that polarization properties are retained despite physical segmentation.

Scenario 4: Even when split cells are spaced further apart horizontally relative to the electric current, they remain coupled for polarization, demonstrating that distance alone in this orientation does not decouple the cells' electrical interaction.

Scenario 5: Changes in the relative cell volume within the domain do not affect the phase response, confirming that variations observed in other scenarios are not influenced by the relative size of the cell within the measurement space.

Scenario 6: Cells enclosed by two membranes exhibit two peak frequencies: one similar to that observed with a single membrane and another ten times higher. However, the polarization at each peak is less intense compared to the single membrane case, reflecting the impact of additional boundaries on charge distribution.

Scenario 7: Reducing the cross-sectional area of the cell results in a lower peak frequency, yet the magnitude of the phase shift remains unchanged. This indicates that while thinner cells alter the frequency of peak polarization, the overall strength of the phase response is similar.

4 DISCUSSION

4.1 Qualitative interpretation of experimental data

In this discussion section, we first qualitatively evaluate the theoretical and numerical findings in comparison with previously published experimental data (Table 2). Previous experiments reported similar magnitudes of phase shift ($|\Phi|$) across different experimental setups. According to our simulations, the maximum $|\Phi|$ generally showed low sensitivity to geometric constraints such as cell size, root size and the proximity of neighbouring cells. This was true with the exception of the double-layer membrane scenario, which we will address later. These factors, which can vary widely among different plant species and growth conditions, seemingly did not affect the maximum $|\Phi|$. Additionally, our theoretical results indicated that membrane properties do not significantly influence the maximum $|\Phi|$. Thus, both the theoretical and simulation outcomes aligned with the experimental observation of a relatively constant maximum $|\Phi|$.

Furthermore, while the ratio of conductivity between the inside and outside of the cell (σ_r) may differ across plants, it does not substantially alter the polarization, as will be further discussed in the following section.

The peak frequency, which is the frequency at which the maximum phase shift occurs, was found to vary more than eight-fold, from 1000 Hz to over 8000 Hz, in prior studies. Our theoretical framework and simulations suggested that the peak frequency can

fluctuate due to factors such as the geometric arrangement of cells, the total length of coupled cells that polarize together, membrane properties and the conductivity of water inside and outside the cells. These factors can differ based on plant types and growth conditions, and the experimental setup itself may influence the length of coupling cells. Therefore, the observed variations in peak frequency across experiments are consistent with our model.

Regarding the double membrane scenario, our simulations identified two smaller peaks of $|\Phi|$, whereas experimental results typically showed only a single peak. Additionally, experimental measurements were conducted at very low frequencies. The implications of this frequency range will be discussed later, but it suggests that the observed polarization may be attributed to either the polarization from a single membrane or the lower peak of the double membrane case, where the peak frequencies are almost identical. Even though the peak $|\Phi|$ in the double membrane scenario was about 65 per cent of that observed in the single membrane case, the magnitudes were within the same order.

For geometric constraints involving double-membrane cells, we expect similar qualitative behaviour to the single-membrane case, provided the same double-membrane cells are used. This is because a double-membrane cell can be considered a single cell with two peak frequencies, and each frequency is simulated independently. A more detailed investigation would require a finer mesh to resolve the space between membranes, posing technical challenges and necessitating a wider range of geometric patterns. Therefore, for approximate comparisons between experimental results and simulation outcomes in the next section, we will not distinguish whether the polarization originates from a double- or single-membrane cell.

4.2 Quantitative comparison to experimental data

In our simulations, results were presented in non-dimensional form. To align these results with experimental observations, we converted non-dimensional frequencies to dimensional frequencies. The parameters for membrane properties and conductivity outside the cell were kept consistent with the theoretical framework, except for the characteristic size. We determined the conversion factor by equating the length of the simulation domain to the distance between electrodes used in the experiments by Ehosioke *et al.* (2023). We set the total simulation domain (10 space units of r') to 3 cm, establishing the characteristic length in our simulations as $L = 0.3$ cm. Using this characteristic length and the parameters discussed earlier, the dimensional frequency was calculated as $f = l\sigma_{\text{out}}\omega^*/4\pi L\varepsilon = 7.2 \times 10^3 \times \omega^*\,(\text{s}^{-1})$.

To qualitatively compare our simulation results with experimental data, we simplified the real root cell configuration as depicted in Fig. 8. We assumed a segment of the root where cells are densely packed and of similar size, arranged regularly. While real cells vary in size and arrangement, our model aims to approximately reproduce experimental outcomes. Furthermore, we assumed that cells aligned along the electric current direction are coupled and can be represented as a single long cell. However, we did not assume all cells are coupled. Due to symmetry with respect to the perpendicular and horizontal direction of the electric field, we only needed to consider one segment.

Building on the discussion above, we utilized results from Scenario 2, where we altered the length of the cell. Although the simulation featured only a single cell, the reasoning about cellular coupling suggests that this single long cell effectively represents a chain of many cells aligned with the direction of the electric current. Therefore, we considered the length of this single cell to represent the entire collective length of the coupled cells.

In our simulation, we assumed equal conductivity inside and outside the cell ($\sigma_r = 1$). However, in reality, the conductivity inside the cell might be slightly higher than outside, though significant variations are unlikely because cells regulate osmotic pressure to minimize stress (Xiao & Zhou 2023). This regulation helps maintain a stable salt concentration ratio between the inside and outside of the cell. To evaluate the impact of different conductivity ratios, we simulated the response for $\sigma_{\text{r}} = 2$ using the longest cell in Scenario 2. Interestingly, the results showed almost the same phase shift on the cell surface as when $\sigma_{\text{r}} = 1$ (Fig. 9a). This outcome can be attributed to the behaviour of the potential gradient across the cell surface. As specified in eqs (50) and (51), σ_{r} influences this gradient. However, in this particular geometric setup, the potential gradient was minimal, leading to similar responses regardless of whether $\sigma_{\text{r}} = 1$ or $\sigma_{\text{r}} = 2$.

Upon converting the non-dimensional frequencies to ordinary frequencies, we found that the peak frequencies varied depending on the coupling length—about 8000 Hz for the shortest and 400 Hz for the longest coupling lengths (Fig. 9a). These values encompass the experimental observations, which range from 1000 to over 8000 Hz (Fig. 9b). The observed peak Φ was approximately 0.3 (rad), around 40 to 55 per cent smaller than experimental values (Fig. 9). This approximation is reasonably accurate, considering that no fitting parameters were used in our straightforward simulation setup, and that we are not trying to reproduce an experiment but to set the foundation of a framework to get a deeper understanding of the fundamental mechanisms behind induced polarization applied to roots.

The discrepancies with experimental results could be linked to the inherent complexity of plant cells. Factors such as cell size, the conductivity of solutions inside and outside the cell, and membrane properties can vary significantly. Moreover, these characteristics are influenced by the specific plant species and environmental conditions, adding layers of variability that are challenging to encapsulate fully in a simulation.

From an experimental perspective, measuring a higher frequency range beyond the usual IP measurement could be beneficial for identifying additional characteristic frequencies. This could suggest multiple characteristic lengths, such as in the double-membrane scenario, though such measurements are challenging. Additionally, controlling plant physiology and ensuring reproducibility are crucial but also experimentally demanding, as they require specialized skills to manage plant growth.

5 CONCLUSION

We have developed a theoretical and numerical model to investigate the polarization of plant cells, with a particular focus on interfacial polarization across the cell membrane. Our model takes into account the densely packed nature of plant root cells within small areas, examining the impact of such geometric constraints through simulations. Notably, our results explain the previously unexplained phenomenon of significant polarization at low frequencies in plant root cells, revealing that the cells can polarize together (i.e., coupling of polarization) within such constricted geometries. Furthermore, by integrating both analytical and simulation findings, we suggest a general guideline for predicting and interpreting the polarization of root cells:

(1) Potentials are highly sensitive to the geometric constraints of cell positioning, with variations exceeding threefold. In contrast, the phase shift is generally less affected by geometry, exhibiting only about a 15 per cent variation, except in specific geometries where two membranes are present. This consistency in phase shift aligns with previous experimental studies, which observed a maximum phase shift variation of approximately 30 per cent.

(2) Unlike the phase shift, the peak frequency is significantly influenced by various factors including membrane properties, cell size, cell arrangement and electrical conductivity. According to theoretical analyses and numerical simulations, the variation in peak frequency can span an order of magnitude. This theoretical range aligns with prior experimental results, where the peak frequency ranged from a low of 1000 Hz to over 8000 Hz.

Additionally, our theoretical and numerical approaches allow for a rough estimation of how polarization response depends on these factors, although precise predictions under geometric constraints may be limited. Overall, the alignment of our theoretical and numerical findings with previous experimental data provides a robust foundation for *in-situ* characterization of plant root systems. Future research can explore additional characteristics of plant roots detectable by polarization response beyond root mass. For example, examining how stress conditions or nutrient uptake alter polarization response through conductivity ratio (σ_r) or how cell death affects polarization response by modifying cell arrangement could yield valuable insights.

The direct application of our simulations to field conditions is limited since our model focuses on a segment of the plant root to understand the inner mechanism of polarization. Simulating actual field conditions would require a significantly larger domain, and different boundary conditions, making it computationally challenging. Moreover, our model does not consider the environmental conditions surrounding the roots nor the rhizosphere. Advancing this approach for field applications would require addressing these two key aspects: large-scale simulations and root-environment interactions. Our theoretical model revealed that the polarization of single microbial cells occurs at a frequency higher than what the induced polarization method can measure. However, when microbes interact with other polarizing sources in geological materials, the resulting polarization might fall within the measurable range of induced polarization (Ntarlagiannis *et al.* 2005; Davis *et al.* 2006; Slater *et al.* 2007; Abdel Aal *et al.* 2009; Zhang *et al.* 2010; Wu *et al.* 2014; Mellage *et al.* 2018). This type of polarization can be modelled using our theoretical and numerical frameworks.

ACKNOWLEDGMENTS

Funding for this research was provided by F.R.S. - FNRS Postdoctoral Fellowship in Belgium (grant No. FC 47069). We acknowledge two reviewers, Dr. Luca Peruzzo in University of Padova and Dr. Léa Lévy in University of Rennes, for their fruitful feedbacks.

DATA AVAILABILITY

The simulation code underlying this article is available in Zenodo, at https://dx.doi.org/10.5281/zenodo.7736461

REFERENCES

Abdel Aal, G., Atekwana, E., Radzikowski, S. & Rossbach, S., 2009. Effect of bacterial adsorption on low frequency electrical properties of clean quartz sands and iron-oxide coated sands, *Geophys. Res. Lett.,* **36,** 1–5.

Abdel Aal, G.Z., Atekwana, E.A. & Revil, A., 2014. Geophysical signatures of disseminated iron minerals: a proxy for understanding subsurface biophysicochemical processes, *J. geophys. Res.: Biogeosci.,* **119,** 1831–1849.

Asami, K., 2006. Dielectric dispersion in biological cells of complex geometry simulated by the three-dimensional finite difference method, *J. Phys. D: Appl. Phys.,* **39**(3), 492–499.

Asami, K., 2007. Dielectric properties of biological tissues in which cells are connected by communicating junctions, *J. Phys. D: Appl. Phys.,* **40**(12), 3718–3727.

Atkinson, J.A., Pound, M.P., Bennett, M.J. & Wells, D.M., 2019. Uncovering the hidden half of plants using new advances in root phenotyping, *Curr. Opin. Biotechnol.,* **55,** 1–8.

Bera, T.K., 2018. Bioelectrical impedance and the frequency dependent current conduction through biological tissues: a short review, *IOP Conf. Ser. Mater. Sci. Eng.,* **331**(1).

Bera, T.K., Nagaraju, J. & Lubineau, G., 2016. Electrical impedance spectroscopy (EIS)-based evaluation of biological tissue phantoms to study multifrequency electrical impedance tomography (Mf-EIT) systems, *J. Vis.,* **19**(4), 691–713.

Breede, K., Kemna, A., Esser, O., Zimmermann, E., Vereecken, H. & Huisman, J.A., 2011. Joint measurement setup for determining spectral induced polarization and soil hydraulic properties, *Vadose Zone J.,* **10**(2), 716–726.

Cao, Y., Repo, T., Silvennoinen, R., Lehto, T. & Pelkonen, P., 2011. Analysis of the willow root system by electrical impedance spectroscopy, *J. Exp. Bot.,* **62**(1), 351–358.

Cimpoiaşu, M.O., Kuras, O., Pridmore, T. & Mooney, S.J., 2020. Potential of geoelectrical methods to monitor root zone processes and structure: A review, *Geoderma,* **365**.

Cseresnyés, I., Rajkai, K. & Vozáry, E., 2013. Role of phase angle measurement in electrical impedance spectroscopy, *Int. Agrophys.,* **27**(4), 377–383.

Cseresnyés, I., Kabos, S., Takács, T., Végh, K.R., Vozáry, E. & Rajkai, K., 2017. An improved formula for evaluating electrical capacitance using the dissipation factor, *Plant Soil,* **419**(1–2), 237–256.

Cseresnyés, I., Szitár, K., Rajkai, K., Füzy, A., Mikó, P., Kovács, R. & Takács, T., 2018. Application of electrical capacitance method for prediction of plant root mass and activity in field-grown crops, *Front. Plant Sci.,* **9**.

Cseresnyés, I., Pokovai, K., Barcza, Z., Marton, T.A. & Fodor, N., 2022. Root electrical capacitance as an indicator of wheat growth and yield in a free-air carbon dioxide enrichment (FACE) experiment, *Plant Soil,* **474**(1-2), 321–335.

Dalton, F.N., 1995. In-situ root extent measurements by electrical capacitance methods, Tech. Rep.

Davis, C.A., Atekwana, E.E., Atekwana, E.E., Slater, L.D., Rossbach, S. & Mormile, M.R., 2006. Microbial growth and biofilm formation in geologic media is detected with complex conductivity measurements, *Geophys. Res. Lett.,* **33**(18), n/a–n/a.

Dietrich, R.C., Bengough, A.G., Jones, H.G. & White, P.J., 2012. A new physical interpretation of plant root capacitance, *J. Exp. Bot.,* **63**(17), 6149–6159.

Ehosioke, S. *et al.*, 2020. Sensing the electrical properties of roots: a review, *Vadose Zone J.,* **19**(1), 1–29.

Ehosioke, S., Garré, S., Huisman, J.A., Zimmermann, E., Placencia-Gomez, E., Javaux, M. & Nguyen, F., 2023. Spectroscopic approach toward unraveling the electrical signature of roots, *J. geophys. Res.: Biogeosci.,* **128**(4).

Feng, L., Li, Q., Cameron, S.D., He, K., Colby, R., Walker, K.M., Deckman, H.W. & Ertaş, D., 2020. Quantifying induced polarization of conductive inclusions in porous media and implications for geophysical measurements, *Sci. Rep.,* **10**(1), 7–11.

Findlay, G., Tyerman, S., Garrill, A. & Skerrett, M., 1994. Pump and K+ inward rectifiers in the plasmalemma of wheat root protoplasts, *J. Membr. Biol.,* **139**(2), 577.

Flores-Cosío, G., Herrera-López, E.J., Arellano-Plaza, M., Gschaedler-Mathis, A., Kirchmayr, M. & Amaya-Delgado, L., 2020. Application of dielectric spectroscopy to unravel the physiological state of microorganisms: current state, prospects and limits, *Appl. Microbiol. Biotechnol.,* **104**(14), 6101–6113.

Griffiths, M. *et al.*, 2022. Optimisation of root traits to provide enhanced ecosystem services in agricultural systems: a focus on cover crops, *Plant Cell Environ.,* **45**(3), 751–770.

Gu, H., Cseresnyés, I., Butnor, J.R., Li, B., Sun, H., Zhang, X., Lu, Y. & Liu, X., 2024. Advancing noninvasive and nondestructive root phenotyping techniques: A two-phase permittivity model for accurate estimation of root volume, *Geoderma,* **442,** 116 773.

Gurin, G., Titov, K., Ilyin, Y. & Tarasov, A., 2015. Induced polarization of disseminated electronically conductive minerals: a semi-empirical model, *Geophys. J. Int.,* **200**(3), 1555–1565.

Hou, L.H. *et al.*, 2022. Use of X-ray tomography for examining root architecture in soils, *Geoderma,* **405,** 115 405.

Izumoto, S., 2023. Induced polarization of metal grains: simulations of three-dimensional electric fields, *J. Geophys. Res. Solid Earth,* **128**(9).

Jócsák, I., Végvári, G. & Vozáry, E., 2019. Electrical impedance measurement on plants: a review with some insights to other fields, *Theor. Exp. Plant Physiol.,* **31**(3), 359–375.

Kessouri, P. *et al.*, 2019. Induced polarization applied to biogeophysics: recent advances and future prospects, *Near Surface Geophys.,* **17**(6), 595–621.

Kotnik, T. & Miklavcic, D., 2000. Second-order model of membrane electric field induced by alternating external electric fields, *IEEE Trans. Biomed. Eng.,* **47**(8), 1074–1081.

Liu, Y., Li, D.M., Qian, J., Di, B., Zhang, G. & Ren, Z.H., 2021. Electrical impedance spectroscopy (EIS) in plant roots research: a review, *Plant Methods,* **17**(1), 1–25.

MacRobert, T., 1967. *Spherical Harmonics: An Elementary Treatise on Harmonic Functions with Applications,* Pergamon Press.

Mancuso, S., ed., 2012. *Measuring Roots,* Springer-Verlag, Berlin.

Mary, B., Abdulsamad, F., Saracco, G., Peyras, L., Vennetier, M., Mériaux, P. & Camerlynck, C., 2017. Improvement of coarse root detection using time and frequency induced polarization: from laboratory to field experiments, *Plant Soil,* **417**(1–2), 243–259.

Mellage, A., Smeaton, C.M., Furman, A., Atekwana, E.A., Rezanezhad, F. & Van Cappellen, P., 2018. Linking spectral induced polarization (SIP) and subsurface microbial processes: Results from sand column incubation experiments, *Environ. Sci. Technol.,* **52**(4), 2081–2090.

Ntarlagiannis, D., Williams, K.H., Slater, L. & Hubbard, S., 2005. Low-frequency electrical response to microbial induced sulfide precipitation, *J. geophys. Res.,* **110,** G02009.

Ozier-Lafontaine, H. & Bajazet, T., 2005. Analysis of root growth by impedance spectroscopy (EIS), *Plant Soil,* **277**(1–2), 299–313.

Parkhurst, D.L. & Appelo, C.A.J., 2013. Description of input and examples for PHREEQC Version 3–a computer program for speciation, batch-reaction, one-dimensional transport, and inverse geochemical calculations.

Peruzzo, L., Schmutz, M., Franceschi, M., Wu, Y. & Hubbard, S.S., 2018. The relative importance of saturated silica sand interfacial and pore fluid geochemistry on the spectral induced polarization response, *J. geophys. Res.: Biogeosci.,* **123**(5), 1702–1718.

Peruzzo, L. *et al.*, 2021. Three-channel electrical impedance spectroscopy for field-scale root phenotyping, *Plant Phenome J.,* **4**(1).

Schwartz, N., Shalem, T. & Furman, A., 2014. The effect of organic acid on the spectral-induced polarization response of soil, *Geophys. J. Int.,* **197**(1), 269–276.

Slater, L., Ntarlagiannis, D., Personna, Y.R. & Hubbard, S., 2007. Pore-scale spectral induced polarization signatures associated with FeS biomineral transformations, *Geophys. Res. Lett.,* **34,** L21404.

Smith, J.R. & Kerr, R.J., 1987. Potassium transport across the membranes of chara, *J. Exp. Bot.,* **38**(5), 788–799.

Stern, H.A. & Feller, S.E., 2003. Calculation of the dielectric permittivity profile for a nonuniform system: application to a lipid bilayer simulation, *J. Chem. Phys.,* **118**(7), 3401–3412.

Taiz, L. & Zeiger, E., 2002. *Plant Physiology,* 3rd ed., Sinauer Associates, Sunderland.

Tracy, S.R., Nagel, K.A., Postma, J.A., Fassbender, H., Wasson, A. & Watt, M., 2020. Crop improvement from phenotyping roots: highlights reveal expanding opportunities, *Trends Plant Sci.,* **25**(1), 105–118.

Tsukanov, K. & Schwartz, N., 2020. Relationship between wheat root properties and its electrical signature using the spectral induced polarization method, *Vadose Zone J.,* **19**(1).

Tsukanov, K. & Schwartz, N., 2021. Modeling plant roots spectral induced polarization signature, *Geophys. Res. Lett.,* **48**(5), 1–8.

Turcan, I. & Olariu, M.A., 2020. Dielectrophoretic manipulation of cancer cells and their electrical characterization, *ACS Comb. Sci.,* **22**(11), 554–578.

Tyerman, S. & Skerrett, I., 1998. Root ion channels and salinity, *Sci. Hortic.,* **78**(1–4), 175–235.

Wang, H., Huisman, J.A., Zimmermann, E. & Vereecken, H., 2021. Experimental design to reduce inductive coupling in spectral electrical impedance tomography (sEIT) measurements, *Geophys. J. Int.,* **225**(1), 222–235.

Wang, H., Huisman, J.A., Zimmermann, E. & Vereecken, H., 2024. Tackling capacitive coupling in broad-band spectral electrical impedance tomography (sEIT) measurements by selecting electrode configurations, *Geophys. J. Int.,* **238**(1), 187–198.

Weigand, M. & Kemna, A., 2017. Multi-frequency electrical impedance tomography as a non-invasive tool to characterize and monitor crop root systems, *Biogeosciences,* **14**(4), 921–939.

Weigand, M. & Kemna, A., 2019. Imaging and functional characterization of crop root systems using spectroscopic electrical impedance measurements, *Plant Soil,* **435**(1-2), 201–224.

Weigand, M., Zimmermann, E., Michels, V., Huisman, J.A. & Kemna, A., 2022. Design and operation of a long-term monitoring system for spectral electrical impedance tomography (sEIT), *Geosci. Instrum. Methods Data Syst.,* **11**(2), 413–433.

Wu, Y., Surasani, V.K., Li, L. & Hubbard, S.S., 2014. Geophysical monitoring and reactive transport simulations of bioclogging processes induced by Leuconostoc mesenteroides, *Geophysics,* **79**(1).

Xiao, F. & Zhou, H., 2023. Plant salt response: perception, signaling, and tolerance, *Front. Plant Sci.,* **13,** 1–16.

Zhang, C., Ntarlagiannis, D., Slater, L. & Doherty, R., 2010. Monitoring microbial sulfate reduction in porous media using multipurpose electrodes, *J. geophys. Res.,* **115,** 1–11.